A dynamic multilevel model for the simulation of the small structures in homogeneous isotropic turbulence

T. Dubois, F. Jauberteau*
Laboratoire de Mathématiques Appliquées,
Université Blaise Pascal and CNRS (UMR 6620), 63177 Aubière, FRANCE.

to appear in *Journal of Scientific Computing*

Abstract

In turbulence simulations, the small scales of motion, even if they carry only a very small percentage of the whole kinetic energy, must be taken into account in order to accurately reproduce the statistical properties of the flows. This induces strong computational restrictions. In an attempt to understand and model the nonlinear interaction between the small and large scales, a dynamic multilevel procedure is proposed and applied to homogeneous turbulence. As in large eddy simulation, filtering operators are used to separate the different scales of the velocity field. In classical models (Smagorinsky), only the large scale equation is resolved. A different approach is proposed here. Indeed, by analyzing the nonlinear interaction terms in the large scale equation, we show that they locally have a very small contribution to the whole dynamic of the flow. We then propose to treat them less accurately. Specific treatments for these terms are achieved by a space and time adaptative procedure; the cut-off value (filter width) which defines the scale separation varies as time evolves. Simulations at Re_λ in the range of 60 to 150 have been performed until statistical steady states are reached, i.e. over long time period. Comparisons with direct simulations (DNS) show that this numerical modeling provides an efficient resolution of the nonlinear interaction term. The multilevel algorithm is shown to be stable ; the corresponding simulated flows reach a statistically steady state very close to the DNS ones. The shape of the energy spectrum functions as well as the characteristic statistical properties of the velocity and its derivatives are accurately recovered.

1 Introduction

Direct numerical simulations of homogeneous turbulent flows have been performed extensively to increase the understanding of the mechanisms involving the small scale structures (intermittency). Results of numerical simulations provide many different ways to investigate turbulent flows. Indeed, important quantities, as high order correlations, can not be easily evaluated in laboratory. By direct numerical simulations (DNS), various details on the small scale behavior can be obtained. Moreover, by comparing results of direct and modeled simulations, the validity and the limits of the closure models can be estimated. Hence, the modeling can be improved and new models can

*e-mail: thdubois, jauber@ucfma.univ-bpclermont.fr

be developed.

In homogeneous turbulence, no boundary layers are present, nor complex geometry. So reasonably high Reynolds number can be reached and the turbulence can be fully developed. Orszag and Patterson [1] have simulated direct numerical simulations of homogeneous turbulence at Reynolds number $Re_\lambda < 30$ and with a resolution of 32^3. Siggia and Patterson [2] have performed DNS at Reynolds number $Re_\lambda \sim 40$ with a resolution of 32^3. At this Reynolds number there is no separation between the energy containing eddies and the small (dissipative) scales. During the subsequent decade, the increase of computer capacities allowed simulations at higher Reynolds numbers for which a small inertial subrange of the energy spectrum exists. Siggia [3] studied the small-scale intermittency in three-dimensional turbulence. The author collected data related to intermittency such as the flatness and related quantities to the first and second velocity derivatives among many others. Kerr in [4] has presented various simulations corresponding to Reynolds numbers Re_λ from 18 to 83 with a number of modes from 32^3 to 128^3. For the 128^3 simulation, the inertial range extended over five modes. The author studied in details the velocity derivative statistics and the statistics of a passive scalar. Correlations of fourth and higher order have been reported. She et al. in [5] studied the dependency of the skewness and flatness factors of the velocity derivatives upon the different scales of motion. Hence, the skewness factor is found to be a large scale property while the flatness is a dissipation range phenomenon.

Vincent and Meneguzzi [6] obtained a simulation at Re_λ of the order of 150 which corresponds to 240^3 unknowns. This result was obtained on a Cray-2 using the four available processors. In this case, the inertial range extended over one decade. The authors confirm that the probability distribution of the velocity derivative is strongly non Gaussian and is close to exponential. Finest resolutions, namely 512^3 modes, have been recently reported by Chen et al. [7] and Jimenez et al. [8]. These simulations were obtained on massively parallel computers. More recently, a 1024^3 simulation was done on a cluster of workstations (Woodward et al. [9]). In [6], the authors reported several statistical quantities and study the spatial structure of the flow. A similar but more detailed analysis was presented in [8].

The choice of the number of unknowns that have to be retained in order to accurately describe the turbulence statistics, as the energy spectrum function and the high order moments of the velocity and its derivatives, is of great importance in DNS. In [4], resolution refinement at fixed Reynolds number was used in order to estimate the suitable mesh size. In [6], the authors analyzed the transfer terms and the energy spectrum while in [8] the effect of the resolution on the high order statistics were measured. It appears that the cut-off wavenumber must be chosen of the order of $2k_d$ where k_d is the wavenumber corresponding to the Kolmogorov scale. This results in very strong computational restrictions on the size of the physical mesh and therefore on the time step. Due to the $k^{-5/3}$ decrease of the energy spectrum function in the inertial range, most of the energy is concentrated in few low modes so that most of the computational effort consists in computing very small scales. Indeed, less than 2% of the computations are required in order to compute the scales corresponding to wavenumber $k \leq k_d/2$. In DNS, all the scales i.e. from the energy-containing through the dissipative ones are computed with the same numerical scheme. However, the small and large scales have different physical characteristics. For instance, the small scales are known to reach a statistically steady state much faster than the large ones.

In an attempt to relax the numerical constraints, we propose here to apply different numerical treatment to the large and small scales. This approach steams from the dynamical system theory and from mathematical results on the Navier-Stokes equations. Foias, Manley and Temam [10] have derived rigorous mathematical estimates on some quantities related to the small scales in energy and enstrophy norm. They are consistent with the phenomenological theory of 2D turbulence (Kraichnan). Based on these results, new mathematical objects have been constructed, namely the approximate inertial manifolds (AIM). They provide an explicit expression of the small scales as a function of the large ones, modeling the interaction between the different wavelengths. In relation with these developments, an adaptative numerical strategy has been developed by Jauberteau [11], Dubois et al. [12] and Debussche et al. [13]. This strategy consists in computing the small scales, associated with the high wavenumber coefficients of the velocity, and the nonlinear interaction term with less accuracy than the large ones. Essential in this method is the adaptative treatment with time of the cut-off wavenumbers defining the scale separation. This numerical modeling provides a good resolution of the interaction between the resolved scales and the modeled ones in the neighborhood of the cut-off wavenumber. No eddy viscosity is used in the large scale equations, so that no artificial diffusion is introduced.

The feasibility of the method has been shown in Jauberteau et al. [14], [15] and Dubois et al. [12], where the computed solutions were mainly analytical solutions corresponding to 2D and 3D flows. In Dubois et al. [12] and Debussche et al. [13] more complex two dimensional solutions were simulated for periodic boundary values. In the last paper, the authors derived mathematical estimates which tend to prove that the cut-off levels could be decreased and chosen of the order of the Kolmogorov wavenumber. Here, we propose to go further in this direction and to investigate the efficiency of the method on more realistic three-dimensional flows.

The present paper is organized as follows. In Section 2, the considered problem is described. Characteristic quantities of homogeneous turbulent flows, as the energy spectrum function and several length scales, are briefly defined. The computational method and parameters, related to the forcing terms as well as the initial conditions, are fully detailed. In Section 3, we introduce the filtered (large eddies) and the small scale equations. Moreover, in order to motivate the numerical modeling proposed, we analyze some quantities related to the small scales and to the nonlinear interaction term. This modeling, called dynamic multilevel (DML) method, consists in an adaptative strategy with respect to the cut-off wavenumbers and to the time integration. The spectrum is splitted into three different ranges; a specific treatment is achieved in each of these parts. The time adaptivity of the procedure defining the cut-off levels accurately reproduces the time variations of the subgrid scale tensor. Furthermore, the use of several levels allows to take into account local interactions near the cut-off wavenumber. In Section 4, several error estimates are derived and analyzed. They are used in order to elaborate the DML algorithm. The adaptative strategy is then described in details. Finally, in Section 5, we report and analyze the numerical results corresponding to simulations at four different Reynolds numbers in the range of 60 to 150; DNS and DML simulations with the same initial states and the same set of parameters have been performed until statistically steady states were reached. Global spatial quantities as the kinetic energy, the energy dissipation rate and different length scales are first compared. Then, the comparison is based on the analysis of the energy and enstrophy spectra, the high order moments of the velocity and its derivatives, and the probability density functions.

2 Description of the problem

2.1 The governing equations

Since we are interested in homogeneous turbulent flows, we consider a three-dimensional velocity field $\mathbf{u}(\mathbf{x},t)$, with $\mathbf{x} = (x_1, x_2, x_3)$ and $\mathbf{u}(\mathbf{x},t) = (u_1(\mathbf{x},t), u_2(\mathbf{x},t), u_3(\mathbf{x},t))$, governed by the incompressible Navier-Stokes equations namely

$$\begin{cases} \dfrac{\partial \mathbf{u}}{\partial t} - \nu\Delta\mathbf{u} + \boldsymbol{\omega}\times\mathbf{u} + \frac{1}{2}\boldsymbol{\nabla}|\mathbf{u}|^2 + \boldsymbol{\nabla}p \;=\; \mathbf{f}, \\ \boldsymbol{\nabla}\cdot\mathbf{u} \;=\; 0, \\ \mathbf{u}(\mathbf{x}, t=0) \;=\; \mathbf{u}_0(\mathbf{x}), \end{cases} \tag{2.1}$$

where ν is the kinematic viscosity, $\boldsymbol{\omega}(\mathbf{x},t) = \nabla\times\mathbf{u}(\mathbf{x},t)$ is the vorticity and $p(\mathbf{x},t)$ is the pressure. Here, $|-|$ stands for the Euclidean norm in $\mathbb{R}^n$. The flow is forced by an external volume force $\mathbf{f}(\mathbf{x},t)$ with zero mean value, i.e.

$$\frac{1}{|\Omega|}\int_\Omega \mathbf{f}(\mathbf{x},t)d\mathbf{x} \;=\; 0, \quad \text{for all} \quad t > 0. \tag{2.2}$$

By forcing the equations, a statistically steady state can be reached. Once this state is reached, the integration of the equations over a few time units allows us to collect statistics of velocity (and velocity derivatives) components and time averages can be performed. The comparisons of the DNS and DML simulations (see Section 5) are based on statistical quantities characterizing these steady states.

The velocity field, as well as the pressure and the external force, are assumed to be periodic over a period $\Omega = (0, L_1)^n$, $n = 3$ and $L_1 > 0$. Hence, they can be expanded in Fourier series, namely

$$\mathbf{u}(\mathbf{x},t) = \sum_{\mathbf{k}\in\mathbb{Z}^n, \mathbf{k}\neq 0} \hat{\mathbf{u}}(\mathbf{k},t)e^{\mathbf{i}\mathbf{k}_{L_1}\cdot\mathbf{x}}, \text{ with } \mathbf{k}_{L_1} = \frac{2\pi}{L_1}\mathbf{k}. \tag{2.3}$$

And similarly for $\mathbf{f}(\mathbf{x},t)$ and $p(\mathbf{x},t)$. Here the dot in $\mathbf{k}_{L_1}\cdot\mathbf{x}$ is used for the standard scalar product in $\mathbb{R}^n$.

We now introduce the orthogonal projection P of $(L^2_{\text{per}}(\Omega))^n$ onto the Hilbert space $H = \left\{\boldsymbol{\varphi}\in(L^2_{\text{per}}(\Omega))^n, \boldsymbol{\nabla}\cdot\boldsymbol{\varphi} = 0, \hat{\boldsymbol{\varphi}}(0) = 0\right\}$; P can be easily implemented as follows

$$P\boldsymbol{\varphi}(\mathbf{x}) \;=\; \sum_{\mathbf{k}\in\mathbb{Z}^n, \mathbf{k}\neq 0}\left(\hat{\boldsymbol{\varphi}}(\mathbf{k}) - \frac{\mathbf{k}}{|\mathbf{k}|^2}(\mathbf{k}\cdot\hat{\boldsymbol{\varphi}}(\mathbf{k}))\right)e^{\mathbf{i}\mathbf{k}_{L_1}\cdot\mathbf{x}}, \tag{2.4}$$

for any $\boldsymbol{\varphi}\in(L^2_{\text{per}}(\Omega))^n$. Note that, if $\boldsymbol{\varphi} = \boldsymbol{\nabla}\psi$, then $P\boldsymbol{\varphi} = 0$. Hence, the equations of motion (2.1) reduce to an abstract equation in H, namely:

$$\frac{\partial\mathbf{u}}{\partial t} + \nu A\mathbf{u} + B(\mathbf{u},\mathbf{u}) \;=\; \mathbf{g}, \tag{2.5}$$

where A is the Stokes operator, B is the bilinear form $B(\mathbf{u},\mathbf{u}) = P(\boldsymbol{\omega}\times\mathbf{u})$ and $\mathbf{g} = P\mathbf{f}$. This formulation is very useful in practice and allows to reduce the memory size of the codes (see Section 2.3 hereafter).

2.2 Characteristic quantities of homogeneous turbulent flows

This Section is devoted to the definitions of statistical characteristic quantities of homogeneous turbulent flows. Their computed values obtained from simulations will be presented in Section 5. For reference we used Batchelor [16] and Monin and Yaglom [17].

One of the most important quantity used to characterize homogeneous turbulent flows is the two-point velocity correlation tensor defined by

$$R_{ij}(\mathbf{r}) \;=\; \langle u_i(\mathbf{x})u_j(\mathbf{x}+\mathbf{r})\rangle, \quad \text{for any } \mathbf{r}\in\Omega, \quad i,j=1,\ldots,n, \tag{2.6}$$

where $\langle - \rangle = \frac{1}{|\Omega|}\int_\Omega - \, d\mathbf{x}$. Replacing u_i and u_j by their Fourier expansions in (2.6) shows that

$$R_{ij}(\mathbf{r}) \;=\; \sum_{\mathbf{k}\in\mathbb{Z}^n,\mathbf{k}\neq 0} \overline{\hat{u}_i}(\mathbf{k})\hat{u}_j(\mathbf{k})e^{\mathbf{i}\mathbf{k}_{L_1}\cdot\mathbf{r}}. \tag{2.7}$$

When the flow is assumed to be isotropic (see [16], [17]) the tensor $R_{ij}(\mathbf{r})$ is fully determined by the energy spectrum function $E(k)$ defined by

$$E(k) \;=\; \frac{1}{2}\sum_{\mathbf{k}\in S_{k,\frac{1}{2}}} tr(\hat{R}_{ij}(\mathbf{k})) \;=\; \frac{1}{2}\sum_{\mathbf{k}\in S_{k,\frac{1}{2}}} |\hat{\mathbf{u}}(\mathbf{k})|^2, \quad \text{for any } k\in\mathbb{N}^*, \tag{2.8}$$

where $S_{k,\frac{1}{2}} = \left\{\mathbf{k}\in\mathbb{Z}^n;\ |\mathbf{k}|\in[k-\frac{1}{2},k+\frac{1}{2})\right\}$. Similarly, associated with the vorticity correlation tensor $\Omega_{ij}(\mathbf{r}) = \langle\omega_i(\mathbf{x})\omega_j(\mathbf{x}+\mathbf{r})\rangle$ we define the enstrophy spectrum function $\epsilon(k)$ by

$$\epsilon(k) \;=\; \sum_{\mathbf{k}\in S_{k,\frac{1}{2}}} tr(\hat{\Omega}_{ij}(\mathbf{k})) \;=\; \sum_{\mathbf{k}\in S_{k,\frac{1}{2}}} \frac{4\pi^2}{L_1^2}k^2|\hat{\mathbf{u}}(\mathbf{k})|^2. \tag{2.9}$$

The enstrophy and energy spectrum functions are then related by

$$\frac{8\pi^2}{L_1^2}\left(k-\frac{1}{2}\right)^2 E(k) \;<\; \epsilon(k) \;<\; \frac{8\pi^2}{L_1^2}\left(k+\frac{1}{2}\right)^2 E(k), \quad k>0. \tag{2.10}$$

The kinetic energy K is then related to the energy spectrum function via

$$K = \sum_{k=1}^{+\infty} E(k) = \frac{1}{2}\langle|\mathbf{u}|^2\rangle \tag{2.11}$$

and the energy dissipation rate $\varepsilon = \nu\langle|\boldsymbol{\omega}|^2\rangle$ is related to the enstrophy spectrum function by

$$\varepsilon \;=\; \nu\sum_{k=1}^{+\infty}\epsilon(k) \;=\; \nu\sum_{\mathbf{k}\in\mathbb{Z}^n}\frac{4\pi^2}{L_1^2}k^2|\hat{\mathbf{u}}(\mathbf{k})|^2. \tag{2.12}$$

A characteristic velocity can be associated with K, i.e. $u^2 = \frac{1}{3}\langle|\mathbf{u}|^2\rangle = \frac{2}{3}K$.

A characteristic length scale of the energy-containing eddies is the integral scale

$$L \;=\; \frac{3L_1}{8}\frac{\sum_{k=1}^{+\infty}k^{-1}E(k)}{\sum_{k=1}^{+\infty}E(k)}. \tag{2.13}$$

Associated with L, we define by

$$\tau_e = \frac{L}{u}, \tag{2.14}$$

a time scale characteristic of the energy-containing eddies; τ_e is called the eddy-turnover time. Two other characteristic length scales are defined, namely the Taylor microscale

$$\lambda = \sqrt{5}\left(\frac{\langle|\mathbf{u}|^2\rangle}{\langle|\boldsymbol{\omega}|^2\rangle}\right)^{1/2} \tag{2.15}$$

and the Kolmogorov (or dissipation) scale

$$\eta = \left(\frac{\nu^3}{\varepsilon}\right)^{1/4}. \tag{2.16}$$

The wavenumber $k_L = \left[\frac{L_1}{2\pi L}\right]$ corresponds to the wavenumber where most of the kinetic energy is concentrated. A Reynolds number related to the energy-containing eddies is defined by

$$Re_L = \frac{uL}{\nu}, \tag{2.17}$$

and is called the integral scale Reynolds number.

Associated with λ we define a wavenumber $k_\lambda = \left[\frac{L_1}{2\pi\lambda}\right]$ and a Reynolds number i.e. the Taylor microscale Reynolds number

$$Re_\lambda = \frac{u\lambda}{\nu}. \tag{2.18}$$

Note that, above the Kolmogorov dissipation wavenumber $k_d = \left[\frac{L_1}{2\pi\eta}\right]$, the energy is damped by viscous effects. Hence k_d provides an estimate of the largest wavenumber that should be retained in DNS. In [8], the authors have shown that $k_N \simeq k_d$ is the minimum resolution needed and that $k_N \simeq 2k_d$ is ideal for the convergence of the velocity gradients.

2.3 The computational method

The discretization of (2.5) is achieved by a Fourier pseudo-spectral method. Let N the number of modes retained in each spatial direction, then the classical Galerkin approximation consists in looking for

$$\mathbf{u}_N(\mathbf{x},t) = \sum_{\mathbf{k}\in S_N} \tilde{\mathbf{u}}(\mathbf{k},t)e^{\mathbf{i}\mathbf{k}_{L_1}\cdot\mathbf{x}}, \tag{2.19}$$

which is solution of

$$\frac{\partial \mathbf{u}_N}{\partial t} + \nu A\mathbf{u}_N + P_N B(\mathbf{u}_N,\mathbf{u}_N) = \mathbf{g}_N. \tag{2.20}$$

Here P_N is the othogonal projection onto the space spanned by $e^{\mathbf{i}\mathbf{k}_{L_1}\cdot\mathbf{x}}$, for all $\mathbf{k} \in S_N = \{\mathbf{l} \in \mathbb{Z}^n / |l_i| \leq k_N = \frac{N}{2},\ l_n > 0\}$. The computation of the inertial term is performed via FFT's and the 3/2−rule is used to dealiase. For CPU time and memory requirements, the aliasing was not removed in all simulations. However, N was taken sufficiently large, i.e. $k_N \sim 1.5k_d$, so that the small scales were accurately resolved. In all cases, the aliasing errors are partially eliminated by isotropic truncation.

The time advancement of (2.20) is carried out by an exact integration of the linear term and an explicit Runge-Kutta method of the third order for the nonlinear term. A third order scheme is sufficient to preserve the spectral accuracy; the stability is ensured via a CFL condition

$$\text{cfl}(m) \;=\; \frac{2\pi}{L_1} k_N \Delta t \; u_\infty^m < \alpha, \quad \text{for all} \;\; m \geq 0, \tag{2.21}$$

where $u_\infty^m = Max_{\mathbf{j}\in[1,N]^n} |\mathbf{u}_N(\mathbf{x_j}, t_m)|$; $\mathbf{x_j}$ are the Fourier collocation points and $t_m = m\Delta t$. The scheme is described in details in [12].

The simulations have been performed on a Cray YMP-EL (4 processors) and on a Cray C90 (8 processors). A particular effort has been made to optimize the codes; multi tasked versions have been developed. In order to reduce the memory size, we used the fact that the flow is incompressible. Indeed, instead of storing the three components $(\hat{\varphi}_1(\mathbf{k}), \hat{\varphi}_2(\mathbf{k}), \hat{\varphi}_3(\mathbf{k}))$, $\mathbf{k} \in S_N$, of any flow variable $\hat{\boldsymbol{\varphi}}(\mathbf{k})$ satisfying the continuity equation, we only kept $\hat{\varphi}_1(\mathbf{k})$, $\hat{\varphi}_2(\mathbf{k})$ for $\mathbf{k} \in S_N$ and $\hat{\varphi}_3(\mathbf{k})$ for $k_3 = 0$; the values $\hat{\varphi}_3(\mathbf{k})$ for $\mathbf{k} \in S_N \backslash \{k_3 = 0\}$ are recovered from the continuity equation when needed. Finally, the global memory required by the code is of the order of $10 \times N^3$; a 256^3 simulation then fits in 170 Mwords.
The average performances of the codes are of the order of 485 Mflops per processor for the 128^3 and 256^3 simulations. Moreover, the average number of processors used in multitasking mode is of the order of 4.5 when 6 processors are requested, so that 2.18 Gigaflops are reached.

2.4 The computational parameters

We describe hereafter, the choice of the initial condition and of the external force. We replace from now on the period L_1 by 2π which was used in all simulations.

The phases of the Fourier coefficients of the initial condition are random numbers and its energy spectrum satisfies

$$E(k, t=0) \;=\; \frac{1}{2} \sum_{\mathbf{k}\in S_{k,\frac{1}{2}}} |\hat{\mathbf{u}}(\mathbf{k}, t=0)|^2 \;=\; c_0 k^{-\frac{5}{3}} e^{-(k^2/k_0^2)}, \qquad k = 1, \ldots, k_N, \tag{2.22}$$

where k_0 is a given parameter. The constant c_0 is determined by fixing the viscosity ν and the initial Taylor microscale Reynolds number, namely

$$c_0 \;=\; \frac{1}{2}\sqrt{\frac{3}{5}}\; \nu Re_\lambda(t=0) \; \left(\sum_{k=1}^{k_N} k^{-5/3} e^{-k^2/k_0^2} \right)^{-1} \sqrt{\sum_{\mathbf{k}\in S_N} |\mathbf{k}|^2 |\hat{\mathbf{u}}(\mathbf{k}, t=0)|^2}. \tag{2.23}$$

The Reynolds numbers $Re_\lambda(t=0)$, listed in Table 1, were chosen according to the numerical tests performed by Kerr [4]. An estimate of the parameter k_0 in (2.22) can be obtained by imposing that $k_N \leq \frac{3}{2} k_d$ at $t = 0$. Indeed by recalling (2.10) and (2.16) we easily derive

$$\sum_{k=1}^{k_N} \left(\frac{4}{9} k_N^2 - \sqrt{\frac{3}{5}}\; Re_\lambda \; \left(k + \frac{1}{2}\right)^2 \right) k^{-5/3} e^{-k^2/k_0^2} \;\leq\; 0. \tag{2.24}$$

Table 1:
Computational parameters of the different runs.

Mesh	k_N	$Re_\lambda(t=0)$	$k_0^{\min}$	k_0	$\nu_{\min}$	ν
64^3	32	52	17	15	4.4×10^{-3}	5×10^{-3}
96^3	48	65	19	20	2.9×10^{-3}	3×10^{-3}
128^3	64	97	22	30	1.5×10^{-3}	1.5×10^{-3}

For fixed Re_λ, the above relation is valid for $k_0 \geq k_0^{min}$; the values of k_0^{min} corresponding to the simulations studied in Section 5 as well as our choice of the parameter k_0 are listed in Table 1. Once Re_λ and k_0 are fixed, we have to determine the viscosity ν. From (2.13) and (2.14) we can show that τ_e increased when the viscosity is decreased, namely

$$\tau_e \;\geq\; \frac{3\sqrt{5}}{4}\pi\;(\nu Re_\lambda)^{-1}\sum_{k=1}^{k_N} k^{-8/3}e^{-k^2/k_0^2}\left(\sum_{k,l=1}^{k_N}\left(k+\frac{1}{2}\right)^2(kl)^{-5/3}e^{-(k^2+l^2)/k_0^2}\right)^{-1/2}.$$

Therefore, by bounding the eddy-turnover time at $t=0$ we deduce an estimate for ν; we have imposed that $\tau_e \;\leq\; \frac{3\sqrt{3}\pi}{4}$ so that

$$\nu \;\geq\; \nu_{\min} \;=\; \sqrt{\frac{5}{3}}Re_\lambda^{-1}\sum_{k=1}^{k_N} k^{-8/3}e^{-k^2/k_0^2}\left(\sum_{k,l=1}^{k_N}\left(k+\frac{1}{2}\right)^2(kl)^{-5/3}e^{-(k^2+l^2)/k_0^2}\right)^{-1/2}.$$

The values of $\nu_{\min}$ and ν are listed in Table 1.

As it was done by Kerr [4] and by Vincent and Meneguzzi [6], the flow field is forced in a deterministic way; the volume force $\mathbf{f}(\mathbf{x},t)$ is constant in time $\mathbf{f}(\mathbf{x},t)=\mathbf{f}(\mathbf{x})$. In that way, no randomness is artificially introduced in the system. However, as it was pointed out in [6] this choice of force induces large fluctuations of the kinetic energy and of the energy injection rate. Moreover, the external force acts only on the lowest modes of the velocity field and then leads to the formation of big eddies. By injecting energy on the lowest modes, we can minimize the number of degrees of freedom of the system.

From (2.20), the energy equation can be derived

$$\frac{dK}{dt} \;=\; \langle \mathbf{g}_N \cdot \mathbf{u}_N\rangle - \nu\langle|\boldsymbol{\omega}_N|^2\rangle, \tag{2.25}$$

where $\langle \mathbf{g}_N \cdot \mathbf{u}_N\rangle$ is the energy injection rate. Note that, without forcing, the turbulence is decaying, i.e. K tends towards zero when t tends to $+\infty$. In all simulations, the external volume force is time independent and takes the form

$$\mathbf{g}_N(\mathbf{x}) = \sum_{\mathbf{k}\in S_N}\hat{\mathbf{g}}(\mathbf{k})\delta_{k,1}e^{i\mathbf{k}\cdot\mathbf{x}},$$

where $\hat{g}_j(\mathbf{k}) = |\hat{g}_j(\mathbf{k})|e^{i\theta(\mathbf{k})}$, $j = 1, 2$ or 3 and $\theta(\mathbf{k}) \in [0, 2\pi]$ is randomly generated. The amplitude of the external volume force is chosen so that the energy injection and the dissipation are in balance at $t = 0$, namely

$$\langle \mathbf{g}_N \cdot \mathbf{u}_N(t=0)\rangle \;\simeq\; \nu\langle|\boldsymbol{\omega}_N(t=0)|^2\rangle. \tag{2.26}$$

This avoids strong variations of the energy K during the transition period.

3 Theoretical arguments

3.1 Reformulation of the equations: the spatial filtering

Due to the very large range of length scales at high Reynolds numbers, the direct simulation of a turbulent flow in complete detail remains impossible. A classical approach, proposed by O. Reynolds [18], consists in averaging the Navier-Stokes equations over an ensemble of realizations, over a time interval or over a volume. Such process reduces the dimensionality of the problem. In large eddy simulation (LES), method introduced by Smagorinsky [19], the very oscillated (random) function $\mathbf{u}$ is replaced by a smoother velocity field $\overline{\mathbf{u}}$ obtained by the convolution of $\mathbf{u}$ with a filter function G, namely :

$$\overline{\mathbf{u}}(\mathbf{x}, t) = \int_\Omega \mathbf{u}(\mathbf{x}', t)\, G(\mathbf{x} - \mathbf{x}', \ell)\, d\mathbf{x}', \tag{3.1}$$

where ℓ is a characteristic filter width; note that the filter function G is time independent.
The net effect of (3.1) is to remove the small scale fluctuations of length smaller than ℓ. The averaged velocity $\overline{\mathbf{u}}$ can then fit onto a grid with size of the order of ℓ.
We define the subgrid scale (SGS) velocity by

$$\mathbf{u}'(\mathbf{x}, t) = \mathbf{u}(\mathbf{x}, t) - \overline{\mathbf{u}}(\mathbf{x}, t). \tag{3.2}$$

By applying the operator defined by (3.1) to (2.5), equation for the filtered velocity is derived :

$$\frac{\partial \overline{\mathbf{u}}}{\partial t} + \nu A\overline{\mathbf{u}} + \overline{B(\mathbf{u}, \mathbf{u})} \;=\; \overline{\mathbf{g}}. \tag{3.3}$$

We used in (3.3) the crucial hypothesis that the operator, denoted by the over bar, commutes with differentiations. In (3.3), the nonlinear terms can be rewritten as follows :

$$\overline{B(\mathbf{u}, \mathbf{u})} \;=\; \overline{B(\overline{\mathbf{u}} + \mathbf{u}', \overline{\mathbf{u}} + \mathbf{u}')} \;=\; \overline{B(\overline{\mathbf{u}}, \overline{\mathbf{u}})} + \overline{B_{int}(\overline{\mathbf{u}}, \mathbf{u}')}, \tag{3.4}$$

where

$$B_{int}(\overline{\mathbf{u}}, \mathbf{u}') \;=\; B(\overline{\mathbf{u}}, \mathbf{u}') + B(\mathbf{u}', \overline{\mathbf{u}}) + B(\mathbf{u}', \mathbf{u}') \tag{3.5}$$

represents the subgrid scale interaction between the averaged velocity and the small scale fluctuations. At this point, we want to note that $B_{int}(\overline{\mathbf{u}}, \mathbf{u}')$ can be expressed in terms of the subgrid scale tensor $\boldsymbol{\tau}$ as follows

$$\overline{B_{int}(\overline{\mathbf{u}}, \mathbf{u}')} \;=\; P\,(\boldsymbol{\nabla} \cdot \boldsymbol{\tau})\,,$$

where $\tau_{ij} = (\overline{u'_i \overline{u}_j} + \overline{u'_j \overline{u}_i}) + \overline{u'_i u'_j}$, $i, j = 1, 2, 3$.

The truncation of an infinite Fourier expansion of $\mathbf{u}$, in which all the wavenumbers k larger than a cut-off value k_N are removed, as in (2.19), corresponds to the filter function

$$G_N(\mathbf{x}) = \prod_{i=1}^{n} D_N(x_i), \tag{3.6}$$

where $D_N(x_i)$ is the Dirichlet kernel (see [20]). The projection operator P_N, introduced in (2.20), can be rewritten in terms of the filtration operator, i.e.:

$$\mathbf{u}_N = P_N\mathbf{u} = \int_\Omega G_N(\mathbf{x}-\mathbf{x}')\,\mathbf{u}(\mathbf{x}')\,d\mathbf{x}'. \tag{3.7}$$

If the cut-off value k_N is large enough, i.e. $k_N > k_d$, the fluctuating velocity $\mathbf{u}' = (I - P_N)\mathbf{u}$ is so small that it can be neglected leading to the equation

$$\frac{\partial \mathbf{u}_N}{\partial t} + \nu A\mathbf{u}_N + P_N B(\mathbf{u}_N, \mathbf{u}_N) = P_N\mathbf{g}. \tag{3.8}$$

Note that (3.8) is exactly the Galerkin approximation of (2.5). Hence, a classical pseudo spectral approximation of the Navier-Stokes equations can be considered as a prefiltering method.
Recalling that the dissipation wavenumber k_d is of the order of $k_L(Re_L)^{3/4}$, it clearly appears that (3.8) can only be solved for moderate Reynolds number.

Let us give a cut-off value $k_{N_1} < k_N$ and convolve the filter function G_{N_1} with $\mathbf{u}_N$. We obtain the large scale components of the velocity

$$\mathbf{y}_{N_1}(\mathbf{x},t) = P_{N_1}\mathbf{u}_N = \int_\Omega G_{N_1}(\mathbf{x}-\mathbf{x}')\,\mathbf{u}_N(\mathbf{x}',t)\,d\mathbf{x}', \tag{3.9}$$

and the remaining subgrid scale velocity

$$\mathbf{z}_{N_1}^N(\mathbf{x},t) = Q_{N_1}^N\mathbf{u}_N = (I_N - P_{N_1})\mathbf{u}_N. \tag{3.10}$$

By applying P_{N_1} and $Q_{N_1}^N$ to (3.8), we derive the large scale equation

$$\frac{\partial \mathbf{y}_{N_1}}{\partial t} + \nu A\mathbf{y}_{N_1} + P_{N_1}B(\mathbf{y}_{N_1}, \mathbf{y}_{N_1}) \;=\; P_{N_1}\mathbf{g} - P_{N_1}B_{int}(\mathbf{y}_{N_1}, \mathbf{z}_{N_1}^N), \tag{3.11}$$

and the subgrid scale equation

$$\frac{\partial \mathbf{z}_{N_1}^N}{\partial t} + \nu A\mathbf{z}_{N_1}^N + Q_{N_1}^N B(\mathbf{u}_N, \mathbf{u}_N) \;=\; Q_{N_1}^N\mathbf{g}. \tag{3.12}$$

In LES, only (3.11) is retained; the subgrid scales $\mathbf{z}_{N_1}^N$ are not resolved. The different terms in the right-hand side (RHS) of (3.11) can be computed on the spectral subspace S_{N_1}. Nevertheless, the interaction term $P_{N_1}B_{int}(\mathbf{y}_{N_1}, \mathbf{z}_{N_1}^N)$ depends on $\mathbf{z}_{N_1}^N$ which is unknown on a mesh size larger than $\ell_{N_1} = 1/k_{N_1}$. Hence, in order to solve only (3.11), the subgrid scale tensor $\boldsymbol{\tau}$ should be modeled in terms of the resolvable scales $\mathbf{y}_{N_1}$. The Smagorinsky models [19], based on gradient transport hypothesis, are the most commonly used in LES. They consist in modeling the interaction term by diffusive effects (eddy viscosity assumption) on the large scales. Such models have been extensively used in different physical situations, see for instance Deardorff [21], Schumann [22], Moin and Kim [23], and Erlebacher et al. [24]. Our aim here is different. In DNS, the equations (3.11) and (3.12) are integrated with the same numerical scheme. However, the averaged velocity $\mathbf{y}_{N_1}$ and the subgrid scale velocity $\mathbf{z}_{N_1}^N$ have different order of magnitude and different time behaviors. For instance, it is well known in turbulence theory that the small scales reach a statistical steady state much faster than the large ones (see [16]). Hence, we propose to treat them differently. Essential in this method is a space and time adaptivity of the algorithm.

3.2 Time and space behaviors of the small scales

As in the previous Section, we associate to a cut-off level $k_{N_1} < k_N$ the decomposition

$$\mathbf{u}_N = \mathbf{y}_{N_1} + \mathbf{z}_{N_1}^N. \tag{3.13}$$

We introduce the L^2-norm (energy norm) : $|\boldsymbol{\varphi}(\mathbf{x},t)|_2^2 = |\Omega| \langle |\boldsymbol{\varphi}|^2 \rangle$, for any flow variable $\boldsymbol{\varphi}$. Recalling the Parseval identity, the L^2-norm is related to the Fourier coefficients as follows

$$|\boldsymbol{\varphi}(\mathbf{x},t)|_2^2 = |\Omega| \sum_{\mathbf{k}\in \mathbb{Z}^3} |\hat{\boldsymbol{\varphi}}(\mathbf{k},t)|^2. \tag{3.14}$$

Hence, from (3.14) and from the definitions of the projection operators P_{N_1} and $Q_{N_1}^N$, we deduce that the ratio $|\mathbf{z}_{N_1}^N|_2/|\mathbf{y}_{N_1}|_2$ is a decreasing function of N_1. Moreover, $|\mathbf{z}_{N_1}^N|_2/|\mathbf{y}_{N_1}|_2$ is less than unity for any cut-off wavenumber k_{N_1} and it behaves like $k_{N_1}^{-1}$ for $k_{N_1} \le k_d/3$ (see Figure 1)[1]. Hence, for relatively small cut-off levels, the small scales carry a small percentage of the whole energy. Indeed, for the considered simulation, $|\mathbf{z}_{N_1}^N|_2$ for $k_{N_1} = k_d/3$ represents less that 12% of the total energy of the flow.

By recalling the large scale equation (3.11) we note that $\mathbf{z}_{N_1}^N$ acts on the evolution of $\mathbf{y}_{N_1}$ via the nonlinear interaction term $P_{N_1} B_{int}(\mathbf{y}_{N_1}, \mathbf{z}_{N_1}^N)$. From Figure 1, we deduce that, as previously, the ratio $|P_{N_1} B_{int}(\mathbf{y}_{N_1}, \mathbf{z}_{N_1}^N)|_2/|P_{N_1} B(\mathbf{y}_{N_1}, \mathbf{y}_{N_1})|_2$ is a decreasing function of N_1 and is less than the unity for any cut-off wavenumber. Moreover, it behaves like $k_{N_1}^{-0.8}$ for $k_{N_1} \le k_d/3$. The nonlinear interaction term then represents a small correction to the large scale evolution. The quantity analyzed above are global. A more detailed analysis of the nonlinear interaction can be achieved by considering the following spectrum functions

$$\left\{ \begin{aligned} NL_{int}(k, k_{N_1}) &= \tfrac{1}{2} \sum_{\mathbf{k}\in S_{k,\frac{1}{2}}} |\hat{B}_{int,\mathbf{k}}(\mathbf{y}_{N_1}, \mathbf{z}_{N_1}^N)|^2, \\ NL(k, k_{N_1}) &= \tfrac{1}{2} \sum_{\mathbf{k}\in S_{k,\frac{1}{2}}} |\hat{B}_{\mathbf{k}}(\mathbf{y}_{N_1}, \mathbf{y}_{N_1})|^2, \quad \text{for} \quad 1 \le k \le k_N. \end{aligned} \right. \tag{3.15}$$

We also define the spectrum function

$$T(k) = \frac{1}{2} \sum_{\mathbf{k}\in S_{k,\frac{1}{2}}} |\tilde{\dot{\mathbf{u}}}(\mathbf{k})|^2, \tag{3.16}$$

where $\dot{\mathbf{u}}$ denotes the time derivative $\frac{\partial \mathbf{u}}{\partial t}$. On Figure 2 we note that

$$NL_{int}(k, k_{N_1}) < NL(k, k_{N_1}) \simeq T(k), \quad \text{for} \quad k < k_{N_1}. \tag{3.17}$$

For a fixed k_{N_1}, $NL_{int}(k, k_{N_1})$ is an increasing function of the wavenumber k while $NL(k, k_{N_1})$ remains approximatively constant; moreover, $NL_{int}(k_{N_1}, k_{N_1}) = NL(k_{N_1}, k_{N_1})$. Note that for $k \le k_{N_1}/2$ the nonlinear interaction represents less than 0.5% of the large scale time derivative. Hence, most of the nonlinear interaction occurs near the cut-off wavenumber. As a consequence, the nonlinear interaction term $P_{N_1} B_{int}(\mathbf{y}_{N_1}, \mathbf{z}_{N_1}^N)$, and so the small scales, can not be neglected in the

[1]The Figures 1 to 8 correspond to the 128^3 direct simulation described in details in Section 5.

simulation. The net effect of this term is to maintain the $k^{-5/3}$ decrease of the energy spectrum and to preserve the turbulence statistics of the flow (see [25] for instance).

Nevertheless, the time variations of the small scales as well as of the nonlinear interaction term appear to be small. Indeed, from Figure 3 we deduce that

$$\begin{cases} \Delta t|\dot{\mathbf{z}}^N_{N_1}|_2 \; < \; |\mathbf{z}^N_{N_1}|_2, \\ \Delta t|P_{N_1}\dot{B}_{int}(\mathbf{y}_{N_1},\mathbf{z}^N_{N_1})|_2 \; < \; |P_{N_1}B_{int}(\mathbf{y}_{N_1},\mathbf{z}^N_{N_1})|_2, \quad \text{for } 1 \le k_{N_1} \le k_N. \end{cases} \tag{3.18}$$

As previously, instead of comparing global quantities, we can analyze the spectrum functions of these quantities. We then define

$$\begin{cases} TNL_{int}(k,k_{N_1}) \; = \; \frac{1}{2} \sum\limits_{\mathbf{k}\in S_{k,\frac{1}{2}}} |\dfrac{\partial}{\partial t}\hat{B}_{int,\mathbf{k}}(\mathbf{y}_{N_1},\mathbf{z}^N_{N_1})|^2, \\ TNL(k,k_{N_1}) \; = \; \frac{1}{2} \sum\limits_{\mathbf{k}\in S_{k,\frac{1}{2}}} |\dfrac{\partial}{\partial t}\hat{B}_{\mathbf{k}}(\mathbf{y}_{N_1},\mathbf{y}_{N_1})|^2, \quad \text{for } \; 1 \le k \le k_N. \end{cases} \tag{3.19}$$

As for $NL_{int}(k,k_{N_1})$ and $NL(k,k_{N_1})$, on Figure 4 we note that

$$TNL_{int}(k,k_{N_1}) \; < \; TNL(k,k_{N_1}), \quad \text{for} \quad k < k_{N_1}. \tag{3.20}$$

For a fixed k_{N_1}, $TNL_{int}(k,k_{N_1})$ is an increasing function of the wavenumber k while $TNL(k,k_{N_1})$ remains approximatively constant; moreover, $TNL_{int}(k_{N_1},k_{N_1}) \; = \; TNL(k_{N_1},k_{N_1})$.

In summary, the small scales as well as the interaction term have completely different space and time behavior than the large ones. Moreover, as it has been previously mentioned they can not be neglected in the simulations. A fundamental question arises at this point : can we numerically treat the former quantities in a simplified way ? Namely, can we neglect the time variations of the nonlinear interaction term and of the small scales over small time intervals ? In order to answer this question and to better understand the numerical effect of these terms on the large scale computation, we propose in the next Sections a dynamical multilevel (DML) scheme. In this method, the small scales as well as the interaction term are kept constant over small time intervals (quasi-static approximation). Note that, such numerical treatment reduce the computational efforts required by DNS.

The spectrum function $T(k)$ corresponding to the time derivative of the velocity is increasing for $k \le k_d/4$ and decreasing for larger wavenumbers (see Figure 2). It is then necessary to control the size of the allowable cut-off level used in the scale separation. In the next Section, the error introduced via a quasi-static approximation of the small scales will be estimated and used in order to estimate the cut-off levels.

In order to conclude this Section, we want to link the above study with the phenomenological theory of turbulence. It is well known that the small scales reach a statistically steady state faster than the large ones (see [16], [26]). Indeed, the characteristic time scale $\tau(k)$, associated with each wavenumber k, is a decreasing function of the wavenumber k. Hence, the smallest physical one is associated with the Kolmogorov scale η and can be defined as

$$\tau_d = \left(\nu \frac{4\pi^2}{L_1^2} k_d^2\right)^{-1}.$$

By assuming that $k_N \geq \frac{3}{2}(k_d+1)$ and recalling (2.21), (2.16) and the definition of k_d, we deduce that

$$\tau_d \;\geq\; \frac{3}{2\alpha c_1^{1/4}} \frac{u_\infty}{u} Re_L^{1/4} \Delta t, \tag{3.21}$$

where c_1 is a dimensionless constant of the order of unity. So $\tau_d/\Delta t$ behaves like $Re_L^{1/4}$. Hence, applying a quasi-static approximation to the small scales is not in contradiction with the fact that they have the smallest characteristic time scale.

4 Numerical modeling of the small scale structures

4.1 The adaptative procedure

The time evolution equation (3.11) of the large scale components $\mathbf{y}_{N_i}$ can be rewritten as

$$\frac{\partial}{\partial t}\left(e^{\nu A t}\mathbf{y}_{N_i}(t)\right) \;=\; e^{\nu A t}\left(P_{N_i}\mathbf{g} - P_{N_i}B(\mathbf{y}_{N_i},\mathbf{y}_{N_i})\right) - e^{\nu A t} P_{N_i} B_{int}(\mathbf{y}_{N_i}, \mathbf{z}^N_{N_i}). \tag{4.1}$$

The integration of (4.1) over a time interval $[t_j + (q-1)\Delta t, t_j + q\Delta t]$, $q \geq 1$ and $t_j = j\Delta t$, leads to

$$\begin{aligned} \mathbf{y}_{N_i}(t_j + q\Delta t) \;&=\; e^{-\nu A \Delta t}\mathbf{y}_{N_i}(t_j + (q-1)\Delta t) \\ &+ \int_{t_j+(q-1)\Delta t}^{t_j+q\Delta t} e^{\nu A(t-(t_j+q\Delta t))}\left[P_{N_i}\mathbf{g} - P_{N_i}B(\mathbf{y}_{N_i}(t),\mathbf{y}_{N_i}(t))\right]\, dt \\ &- \int_{t_j+(q-1)\Delta t}^{t_j+q\Delta t} e^{\nu A(t-(t_j+q\Delta t))} P_{N_i} B_{int}(\mathbf{y}_{N_i}(t), \mathbf{z}^N_{N_i}(t))\, dt. \end{aligned} \tag{4.2}$$

As it was suggested in the previous Section, the nonlinear interaction term is integrated via a quasi-static (QS) approximation, namely

$$P_{N_i} B_{int}(\mathbf{y}_{N_i}(t), \mathbf{z}^N_{N_i}(t)) \simeq P_{N_i} B_{int}(\mathbf{y}_{N_i}(t_j), \mathbf{z}^N_{N_i}(t_j)), \quad \text{for every} \quad t \in [t_j, t_j + q\Delta t]. \tag{4.3}$$

By reporting (4.3) into (4.2), the following approximation of the second integral in the RHS is obtained

$$e^{-\nu A q \Delta t} P_{N_i} B_{int}(\mathbf{y}_{N_i}(t_j), \mathbf{z}^N_{N_i}(t_j)) \int_{(q-1)\Delta t}^{q\Delta t} e^{\nu A t} dt.$$

The nonlinear interaction term then appears as a subgrid source term; indeed, the resulting equation for $\mathbf{y}_{N_i}(t_j + q\Delta t)$ can be solved on the spectral subspace S_{N_i}.
The error induced by such approximation is exactly

$$\int_{t_j+(q-1)\Delta t}^{t_j+q\Delta t} e^{\nu A(t-(t_j+q\Delta t))}\left[P_{N_i} B_{int}(\mathbf{y}_{N_i}(t), \mathbf{z}^N_{N_i}(t)) - P_{N_i} B_{int}(\mathbf{y}_{N_i}(t_j), \mathbf{z}^N_{N_i}(t_j))\right]\, dt, \tag{4.4}$$

which can be bounded as follows

$$|(4.4)|_2 \;\leq\; q\Delta t^2 \max_{t\in[t_j,t_j+q\Delta t]} |P_{N_i}\dot{B}_{int}(\mathbf{y}_{N_i}(t),\mathbf{z}^N_{N_i}(t))|_2. \tag{4.5}$$

Let us assume for instance that, on the time interval $[t_j, t_j+q\Delta t]$, the small scale fluctuations $\mathbf{z}^N_{N_i}(t)$ are frozen, namely we define the following approximation

$$\mathbf{z}^N_{N_i}(t) \simeq \mathbf{z}^N_{N_i}(t_j), \quad \text{for every} \quad t\in[t_j,t_j+q\Delta t]. \tag{4.6}$$

This treatment induces an error which can be estimated as follows

$$\max_{t\in[t_j,t_j+q\Delta t]} |\mathbf{z}^N_{N_i}(t)-\mathbf{z}^N_{N_i}(t_j)|_2 \leq q\Delta t \max_{t\in[t_j,t_j+q\Delta t]} |\dot{\mathbf{z}}^N_{N_i}(t)|_2. \tag{4.7}$$

We now denote

$$\begin{cases} \xi_1(N_i,q) &= q\Delta t^2 \displaystyle\max_{t\in[t_j,t_j+q\Delta t]} |P_{N_i}\dot{B}_{int}(\mathbf{y}_{N_i}(t),\mathbf{z}^N_{N_i}(t))|_2, \\ \xi_2(N_i,q) &= q\Delta t \displaystyle\max_{t\in[t_j,t_j+q\Delta t]} |\dot{\mathbf{z}}^N_{N_i}(t)|_2. \end{cases}$$

As $|\dot{\mathbf{z}}^N_{N_i}(t)|_2$ is by definition a decreasing function of N_i then

$$\xi_2(N_l,q) \;<\; \xi_2(N_i,q), \quad \text{for any level} \quad N_l > N_i. \tag{4.8}$$

Then, by defining $q_l = \left[\frac{\xi_2(N_i,1)}{\xi_2(N_l,1)}\right]$ we have

$$\xi_2(N_l,q_l) \;<\; \xi_2(N_i,1) \;<\; \xi_2(N_l,q_l+1).$$

Hence, for a similar error (i.e. of the same order of magnitude), the small scales corresponding to the level N_l, i.e. $\mathbf{z}^N_{N_l}$ can remain frozen on longer time interval than $\mathbf{z}^N_{N_i}$. The ratio $\xi_2(k_d/2,1)/\xi_2(N_l,1)$ for $N_l > \frac{k_d}{2}$, defining q_l, is increasing and presents strong variations at large wavenumbers (Figure 5). Hence, a natural way to take into account this behavior of $\xi_2(N_l,q)$ is to define different cut-off levels and to increase the length of the QS approximation for the higher levels. This can be achieved by the use of classical multigrid V-cycles described in the next Section.

Moreover, by comparing the time derivatives of the small scales and of the nonlinear interaction term, we note that for a level k_{N_i} the error induced by a QS approximation of $\mathbf{z}^N_{N_i}$ is more restrictive than the one induced by a QS approximation of $P_{N_i}B_{int}(\mathbf{y}_{N_i},\mathbf{z}^N_{N_i})$. Indeed, for a similar error on a cut-off level k_{N_i}, the ratio between the allowable number of iterations of the QS approximation of $P_{N_i}B_{int}(\mathbf{y}_{N_i},\mathbf{z}^N_{N_i})$ and the allowable number of iterations of the QS approximation of $\mathbf{z}^N_{N_i}$ can be estimated by

$$\frac{k_N u_\infty(t_j)|\dot{\mathbf{z}}^N_{N_i}(t_j)|_2}{|P_{N_i}\dot{B}_{int}(\mathbf{y}_{N_i}(t_j),\mathbf{z}^N_{N_i}(t_j))|_2},$$

which is much larger than unity (see Figure 6). Hence, it appears that the nonlinear interaction term can be frozen over much longer time interval than the corresponding small scales.

4.2 The numerical integration of the large and intermediate scales

Let us give a sequence of m cut-off levels $\{N_j\}_{j=1,\dots,m}$ such that $N_j < N_{j'} < N_m = N$ for $m > j' > j \geq 1$. Let us assume that an approximation $\mathbf{w}_N^j$ of the solution of (2.5) is known at the time $t_j = j\Delta t,\ j \geq 0$. We estimate a subsequence of cut-off levels $\{N_{i(j)+l}\},\ l = 0,\dots,p(j)$. For the sake of simplicity we denote $s(j) = i(j) + p(j)$. The approximated velocity field $\mathbf{w}_N^j$ can be decomposed as

$$\mathbf{w}_N^j \ = \ \mathbf{y}_{N_{i(j)}}^j \ + \ \mathbf{z}_{N_{i(j)}}^{N_{s(j)},j} \ + \ \mathbf{r}_{N_{s(j)}}^j, \tag{4.9}$$

where $\mathbf{y}_{N_{i(j)}}^j = P_{N_{i(j)}}\mathbf{w}_N^j$, $\mathbf{z}_{N_{i(j)}}^{N_{s(j)},j} = Q_{N_{i(j)}}^{N_{s(j)}}\mathbf{w}_N^j$ and $\mathbf{r}_{N_{s(j)}}^j = Q_{N_{s(j)}}^N\mathbf{w}_N^j$.

At each time iteration $t_{j+l},\ 1 \leq l \leq 2p(j)$, we associate the cut-off level $N_{\varphi(l)}$, with $\varphi(l) = i(j) + |l - p(j)|$. The large scales $\mathbf{y}_{N_{i(j)}}^{j+l} + \mathbf{z}_{N_{i(j)}}^{N_{\varphi(l)},j+l}$ are computed by approximating their evolution equation (4.1) integrated over the time interval $[t_{j+l-1}, t_{j+l}]$, while a QS approximation is applied to the small scales i.e.

$$Q_{N_{\varphi(l)}}^{N_{s(j)}}\mathbf{w}_N^{j+l} \ = \ Q_{N_{\varphi(l)}}^{N_{s(j)}}\mathbf{w}_N^{j+l-1}. \tag{4.10}$$

This treatment implies that the scales corresponding to wavenumbers $k \in (N_{i(j)+l}/2, N_{i(j)+l+1}/2]$, for $l = 0,\dots,p(j)-1$ are kept constant on the time interval $[t_{j+p(j)-(l+1)}, t_{j+p(j)+l}]$, which corresponds to $2l+1$ time iterations. According to the estimate (4.7), the errors induced by this numerical procedure are bounded by

$$(2l+1)\ \Delta t \max_{t\in[t_{j+p(j)-(l+1)},t_{j+p(j)+l}]} |\dot{\mathbf{z}}_{N_{i(j)+l}}^{N_{i(j)+l+1}}(t)|_2, \quad \text{for } l = 0,\dots,p(j)-1. \tag{4.11}$$

In order to control these errors, we introduce a given non-dimensional parameter $\zeta,\ 0 < \zeta < 1$, and we associate to ζ the quantity $\zeta_j = \zeta \times |\mathbf{w}_N^j|_2$; ζ_j represents an error in L^2-norm. Then, we impose that

$$(2l+1)\ \Delta t\ |\dot{\mathbf{z}}_{N_{i(j)+l}}^{N_{i(j)+l+1},j}|_2 \ < \ \zeta_j, \quad \text{for} \quad l = 0,\dots,p(j)-1, \tag{4.12}$$

so that (4.12) provides a set of constraints on the allowable cut-off levels $\{N_{i(j)+l}\}_{l=0,\dots,p(j)}$. Note that due to the fast decrease of $|Q_{N_1}^N\dot{\mathbf{u}}_N|_2$ for $k_{N_1} > \frac{k_d}{4}$ (see Section 3.2), subsequences of cut-off levels satisfying (4.12) exist. Moreover, in that case, (4.12) reduces to

$$\left\{\begin{array}{l} \Delta t\ |\dot{\mathbf{z}}_{N_{i(j)}}^{N_{i(j)+1},j}|_2 \ < \ \zeta_j, \\ (2p(j)-1)\Delta t\ |\dot{\mathbf{z}}_{N_{s(j)-1}}^{N_{s(j)},j}|_2 \ < \ \zeta_j. \end{array}\right. \tag{4.13}$$

We now describe the computation of the large and intermediate scales on the time interval $[t_j, t_j + 2p(j)\Delta t]$ corresponding to one V-cycle. At the time t_{j+l} the large scales $\mathbf{y}_{N_{i(j)}}^{j+l}$ as well as the intermediate scales $\mathbf{z}_{N_{i(j)}}^{N_{\varphi(l)},j+l}$ are computed by approximating (4.2) with N_i replaced by $N_{\varphi(l)}$ and $[t_j + (q-1)\Delta t, t_j + q\Delta t]$ by $[t_{j+l-1}, t_{j+l}]$, namely

$$\begin{aligned} \mathbf{y}_{N_{i(j)}}^{j+l} \ &+\mathbf{z}_{N_{i(j)}}^{N_{\varphi(l)},j+l} \ = \ e^{-\nu A\Delta t}\left(\mathbf{y}_{N_{i(j)}}^{j+l-1} + \mathbf{z}_{N_{i(j)}}^{N_{\varphi(l)},j+l-1}\right) \\ &+ \Delta t\ e^{-\nu A\Delta t}\left[P_{N_{\varphi(l)}}\mathbf{g} - P_{N_{\varphi(l)}}B(\mathbf{y}_{N_{i(j)}}^{j+l-1} + \mathbf{z}_{N_{i(j)}}^{N_{\varphi(l)},j+l-1}, \mathbf{y}_{N_{i(j)}}^{j+l-1} + \mathbf{z}_{N_{i(j)}}^{N_{\varphi(l)},j+l-1})\right] \\ &- \Delta t\ e^{-\nu A\Delta t}P_{N_{\varphi(l)}}B_{int}(\mathbf{y}_{N_{i(j)}}^j + \mathbf{z}_{N_{i(j)}}^{N_{\varphi(l)},j}, \mathbf{z}_{N_{\varphi(l)}}^{N_{s(j)},j} + \mathbf{r}_{N_{s(j)}}^j). \end{aligned} \tag{4.14}$$

In fact, the nonlinear term in the first integral of (4.2) is integrated by using an explicit third order Runge-Kutta scheme. However, for the sake of simplicity, we used a backward Euler scheme in (4.14). Note that in (4.14), QS approximations are applied to the nonlinear interaction term corresponding to each cut-off level $N_{i(j)+l},\ l = 0,\dots,p(j)$, on the time interval $[t_j, t_{j+p(j)+l}]$. This induces the following errors

$$(p(j)+l)\ \Delta t^2 \max_{t\in[t_j,t_{j+p(j)+l}]} |P_{N_{i(j)+l}} \dot{B}_{int}(\mathbf{y}_{N_{i(j)}}(t) + \mathbf{z}_{N_{i(j)}}^{N_{i(j)+l}}(t), \mathbf{z}_{N_{i(j)+l}}^{N_{s(j)}}(t) + \mathbf{r}_{N_{s(j)}}(t))|_2, \tag{4.15}$$

for $l = 0,\dots,p(j)$. In the DML procedure, we impose the following constraints on the cut-off levels

$$2p(j)\ \Delta t^2 \max_{l=0,\dots,p(j)} |P_{N_{i(j)+l}} \dot{B}_{int}(\mathbf{y}^j_{N_{i(j)}} + \mathbf{z}_{N_{i(j)}}^{N_{i(j)+l},j}, \mathbf{z}_{N_{i(j)+l}}^{N_{s(j)},j} + \mathbf{r}^j_{N_{s(j)}})|_2 \ <\ \zeta_j. \tag{4.16}$$

Note that, according to the behavior of the time derivative of the nonlinear interaction term (see Figure 7), the above constraints reduce to

$$2p(j)\ \Delta t^2\ |P_{N_{i(j)}} \dot{B}_{int}(\mathbf{y}^j_{N_{i(j)}}, \mathbf{z}_{N_{i(j)}}^{N_{s(j)},j} + \mathbf{r}^j_{N_{s(j)}})|_2 \ <\ \zeta_j, \quad \text{for}\ \ k_{N_{i(j)}} \geq \frac{k_d}{2}.$$

As it was noted in Section 4.1, the nonlinear interaction term can remain frozen on time intervals much longer than their corresponding small scales; indeed, the set of constraints (4.15) is less restrictive than (4.12). Hence, we propose to repeat several V-cycles with the same cut-off levels satisfying (4.12). Let us denote by $n_V(j)$ the number of repeated V-cycles. In this case, the time interval of the QS approximation of the nonlinear interaction term becomes $I_{j,l} = [t_j, t_{j+(2n_V(j)-1)p(j)+l}]$ so that (4.15) rewrites

$$((2n_V(j)-1)p(j)+l)\ \Delta t^2 \max_{t\in I_{j,l}} |P_{N_{i(j)+l}} \dot{B}_{int}(\mathbf{y}_{N_{i(j)}}(t) + \mathbf{z}_{N_{i(j)}}^{N_{i(j)+l}}(t), \mathbf{z}_{N_{i(j)+l}}^{N_{s(j)}}(t) + \mathbf{r}_{N_{s(j)}}(t))|_2, \tag{4.17}$$

for $l = 0,\dots,p(j)$. We then impose

$$2n_V(j)p(j)\ \Delta t^2 \max_{l=0,\dots,p(j)} |P_{N_{i(j)+l}} \dot{B}_{int}(\mathbf{y}^j_{N_{i(j)}} + \mathbf{z}_{N_{i(j)}}^{N_{i(j)+l},j}, \mathbf{z}_{N_{i(j)+l}}^{N_{s(j)},j} + \mathbf{r}^j_{N_{s(j)}})|_2 \ <\ \zeta_j. \tag{4.18}$$

As previously, this reduces to

$$2n_V(j)\ p(j)\ \Delta t^2\ |P_{N_{i(j)}} \dot{B}_{int}(\mathbf{y}^j_{N_{i(j)}}, \mathbf{z}_{N_{i(j)}}^{N_{s(j)},j} + \mathbf{r}^j_{N_{s(j)}})|_2 \ <\ \zeta_j, \quad \text{for}\ k_{N_{i(j)}} \geq \frac{k_d}{2}.$$

In summary, a V-cycle consists of $2p(j)$ time iterations on the time interval $[t_j, t_j + 2p(j)\Delta t]$. The current cut-off level varies and is given as a function of the time iteration by $\varphi(l),\ l = 1,\dots,2p(j)$. In order to fully describe the DML procedure introduced above, we define a cycle j corresponding to the time interval $[\tau_j, \tau_{j+1}]$ where

$$\tau_{j+1}\ =\ \tau_j\ +\ 2n_V(j)p(j)\Delta t,\ \ \tau_0\ =\ 0, \tag{4.19}$$

which can be rewritten as

$$\tau_j\ =\ n_j\Delta t,\ \ \text{with}\ \ n_j\ =\ 2\sum_{l=0}^{j-1} p(l)n_V(l),\ \ n_0 = 0.$$

We denote $\tau_{j,l} = \tau_j + 2lp(j)\Delta t$ and $n_{j,l} = n_j + 2lp(j)$ so that $\tau_{j,l} = n_{j,l}\Delta t$ for $l = 0, \dots, n_V(j)$. Note that by definition, $\tau_{j,n_V(j)} = \tau_{j+1}$.

The time interval $[\tau_j, \tau_{j+1}]$ can then be rewritten as $\displaystyle\bigcup_{l=0}^{n_V(j)-1} [\tau_{j,l}, \tau_{j,l+1}]$ and each interval $[\tau_{j,l}, \tau_{j,l+1}]$ corresponds to a V-cycle of length $2p(j)\Delta t$. Then, the approximation of (2.5) by the DML procedure described above consists in performing successive such cycles.

4.3 The numerical integration of the small scales

In Section 4.2, the computation of the small scales corresponding to wavenumbers $k \in (k_{N_{s(j)}}, k_N]$ over the time interval $[\tau_j, \tau_{j+1}]$ is not described. In fact, these scales are reevaluated at the end of each V-cycles, i.e. at each time $\tau_{j,l}$, as a function of the larger scales namely

$$\begin{aligned} \mathbf{r}_{N_{s(j)}}^{n_{j,l}} &= e^{-\nu A 2p(j)\Delta t}\ \mathbf{r}_{N_{s(j)}}^{n_{j,l-1}} \\ &- p(j)\ \Delta t\ \Big[Q_{N_{s(j)}}^N B(\mathbf{y}_{N_{i(j)}}^{n_{j,l}} + \mathbf{z}_{N_{i(j)}}^{N_{s(j)},n_{j,l}}, \mathbf{y}_{N_{i(j)}}^{n_{j,l}} + \mathbf{z}_{N_{i(j)}}^{N_{s(j)},n_{j,l}}) \\ &\quad + e^{-\nu A 2p(j)\Delta t}\ Q_{N_{s(j)}}^N B(\mathbf{y}_{N_{i(j)}}^{n_{j,l-1}} + \mathbf{z}_{N_{i(j)}}^{N_{s(j)},n_{j,l-1}}, \mathbf{y}_{N_{i(j)}}^{n_{j,l-1}} + \mathbf{z}_{N_{i(j)}}^{N_{s(j)},n_{j,l-1}}) \Big], \end{aligned} \tag{4.20}$$

for $l = 1, \dots, n_V(j)$. Note that (4.20) corresponds to an approximation of the integration of the evolution equation (3.12) of $\mathbf{r}_{N_{s(j)}} = Q_{N_{s(j)}}^N \mathbf{u}_N$ over the interval $[\tau_{j,l-1}, \tau_{j,l}]$ where the term $Q_{N_{s(j)}}^N B_{int}(\mathbf{y}_{N_{i(j)}} + \mathbf{z}_{N_{i(j)}}^{N_{s(j)}}, \mathbf{r}_{N_{s(j)}})$ has been neglected and the nonlinear term has been integrated with a Crank-Nicholson scheme. This induces an error which can be estimated as

$$\int_{\tau_{j,l-1}}^{\tau_{j,l}} e^{\nu A(t-\tau_{j,l})} Q_{N_{s(j)}}^N B_{int}(\mathbf{y}_{N_{i(j)}}(t) + \mathbf{z}_{N_{i(j)}}^{N_{s(j)}}(t), \mathbf{r}_{N_{s(j)}}(t))\ dt \tag{4.21}$$

and bounded by (see Figure 2)

$$\begin{aligned} |(4.21)|_2 &\le 2p(j)\ \Delta t \max_{t\in[\tau_{j,l-1},\tau_{j,l}]} |Q_{N_{s(j)}}^N B_{int}(\mathbf{y}_{N_{i(j)}}(t) + \mathbf{z}_{N_{i(j)}}^{N_{s(j)}}(t), \mathbf{r}_{N_{s(j)}}(t))|_2 \\ &\le 2p(j)\ \Delta t \max_{t\in[\tau_{j,l-1},\tau_{j,l}]} |\dot{\mathbf{r}}_{N_{s(j)}}(t)|_2. \end{aligned} \tag{4.22}$$

The numerical model proposed here for the subgrid scale tensor provides a good description of the interaction between the resolved scales and the small scales; neither energy accumulations on the truncated levels nor an excessive dissipation have been observed (see Section 5).

4.4 Summary of the algorithm

We summarize here the procedure described in the previous Sections. We first initialize :

$$\tau_0 = 0\ ,\ n_0 = 0\ ,\ j = 0.$$

We give us the non-dimensional parameter ζ, $0 < \zeta < 1$. We recall that ζ is a non-dimensional parameter corresponding to a relative error in L^2-norm.

Step 1: Computation of the absolute error $\zeta_j = \zeta \times |\mathbf{w}_N^{n_j}|_2$.

Step 2: Computation of the subsequences $\{N_{i(j)+l}\}_{l=0,\ldots,p(j)}$ of cut-off levels so that

$$\left\{ \begin{array}{l} \mathrm{Tol}_1\ \Delta t\ |\dot{\mathbf{z}}_{N_{i(j)}}^{N_{i(j)+1},n_j}|_2\ <\ \zeta_j, \\ 2p(j)\ \mathrm{Tol}_2\ \Delta t\ |\dot{\mathbf{r}}_{N_{s(j)}}^{n_j}|_2\ <\ \zeta_j, \end{array} \right. \tag{4.23}$$

where Tol_1 and Tol_2 are two given parameters of the order of the unity. An additional constraint is imposed i.e. : $p(j) \leq nb_{\mathrm{level}}$, where nb_{level} is a given parameter ($\simeq 5$).

Step 3: Computation of the possible number of repeated V-cycles

$$n_V(j)\ =\ \left[\frac{\zeta_j}{2p(j)\Delta t^2 |P_{N_{i(j)}} \dot{B}_{int}(\mathbf{y}_{N_{i(j)}}^{n_j}, \mathbf{z}_{N_{i(j)}}^{N_{s(j)},n_j} + \mathbf{r}_{N_{s(j)}}^{n_j})|_2} \right]. \tag{4.24}$$

Step 4: Computation and storage of the nonlinear interaction terms corresponding to the cut-off levels $\{N_{i(j)+l}\}_{l=0,\ldots,p(j)}$, namely

$$\begin{aligned} P_{N_{i(j)+l}} B_{int}(\mathbf{y}_{N_{i(j)}}^{n_j} + \mathbf{z}_{N_{i(j)}}^{N_{i(j)+l},n_j}, \mathbf{z}_{N_{i(j)+l}}^{N_{s(j)},n_j} + \mathbf{r}_{N_{s(j)}}^{n_j})\ &=\ P_{N_{i(j)+l}} B(\mathbf{w}_N^{n_j}, \mathbf{w}_N^{n_j}) \\ &-\ P_{N_{i(j)+l}} B(\mathbf{y}_{N_{i(j)}}^{n_j} + \mathbf{z}_{N_{i(j)}}^{N_{i(j)+l},n_j}, \mathbf{y}_{N_{i(j)}}^{n_j} + \mathbf{z}_{N_{i(j)}}^{N_{i(j)+l},n_j}), \end{aligned} \tag{4.25}$$

for $l = 0, \ldots, p(j)$.

Step 5: This step consists in computing the large and small scales on the time interval $\displaystyle\bigcup_{q=0}^{n_V(j)-1} [\tau_{j,q}, \tau_{j,q+1}]$.

This is achieved as it follows :

5-1) $q = 0$;

5-2) $n_{j,q} = n_j + 2qp(j)$;

5-3) for $l = 1, \ldots, 2p(j)$, we define $\varphi(l) = i(j) + |l - p(j)|$ and compute $\mathbf{y}_{N_{i(j)}}^{n_{j,q}+l} + \mathbf{z}_{N_{i(j)}}^{N_{\varphi(l)},n_{j,q}+l}$ according to (4.14) where j is replaced by $n_{j,q}$;

5-4) the small scales $\mathbf{r}_{N_{s(j)}}^{n_{j,q+1}} = \mathbf{r}_{N_{s(j)}}^{n_{j,q}+2p(j)}$ are computed according to (4.20);

5-5) ($q \Leftarrow q + 1$) and return to 5-2) while $q < n_V(j)$.

Step 6: At the time $\tau_{j+1} = \tau_j + 2p(j)n_V(j)\Delta t$, we set : $n_{j+1} = n_j + 2p(j)n_V(j)$. Then, return to Step 1 with ($j \Leftarrow j + 1$).

Note that in practice we never compute $P_{N_{i(j)}} \dot{B}_{int}(\mathbf{y}_{N_{i(j)}}^{n_j}, \mathbf{z}_{N_{i(j)}}^{N_{s(j)},n_j} + \mathbf{r}_{N_{s(j)}}^{n_j})$ which requires a total of $O(N^3 \log_2(N))$ operations. We use the following approximation (see Figure 8)

$$|P_{N_{i(j)}} \dot{B}_{int}(\mathbf{y}_{N_{i(j)}}^{n_j}, \mathbf{z}_{N_{i(j)}}^{N_{s(j)},n_j} + \mathbf{r}_{N_{s(j)}}^{n_j})|_2 \simeq \frac{|Q_{N_{i(j)}}^N \dot{\mathbf{w}}_N^{n_j}|_2\ ||Q_{N_{i(j)}}^N \mathbf{w}_N^{n_j}||}{4\ |Q_{N_{i(j)}}^N \mathbf{w}_N^{n_j}|_2\ ||\mathbf{y}_{N_{i(j)}}^{n_j}||}\ |P_{N_{i(j)}} B(\mathbf{y}_{N_{i(j)}}^{n_j}, \mathbf{y}_{N_{i(j)}}^{n_j})|_2, \tag{4.26}$$

where $||\boldsymbol{\varphi}||^2 = \frac{1}{|\Omega|}\langle|\boldsymbol{\nabla}\boldsymbol{\varphi}|^2\rangle$.

The computation of the nonlinear term on the spectral grid S_{N_i} requires 6 three-dimensional complex-real FFT and 3 real-complex three-dimensional FFT, which represents $9c_2 N_i^3 log_2(N_i)$ floating point operations, where c_2 is a constant. Then, Step 4 in the previous algorithm requires

$$9c_2 N^3 log_2(N) \ + \ 9c_2 \sum_{l=i(j)}^{s(j)} N_l^3 log_2(N_l)$$

floating point operations. Each V-cycle, i.e. Step 5-2) to Step 5-4) for a fixed value of q, requires

$$27c_2 \ N_{i(j)}^3 log_2(N_{i(j)}) \ + \ 54c_2 \sum_{l=i(j)+1}^{s(j)-1} N_l^3 log_2(N_l) \ + \ 27c_2 \ N_{s(j)}^3 log_2(N_{s(j)}) \ + \ 9c_2 N^3 log_2(N)$$

floating point operations except for the first V-cycle which requires $27c_2 N_{i(j)}^3 log_2(N_{i(j)})$ less operations. Hence, the total number of operations of a cycle j is equal to

$$\begin{aligned} 27c_2 \ n_V(j) N_{i(j)}^3 log_2(N_{i(j)}) \ + \ 9c_2(6n_V(j)+1) \sum_{l=i(j)+1}^{s(j)-1} N_l^3 log_2(N_l) \\ + \ 9c_2(3n_V(j)+1) N_{s(j)}^3 log_2(N_{s(j)}) \ + \ 9c_2 \ (n_V(j)+1) N^3 log_2(N). \end{aligned} \tag{4.27}$$

This has to be compared with $54c_2 \ p(j) n_V(j) N^3 log_2(N)$ for a direct simulation on the spectral grid S_N.

Finally, we want to note that the storage of the nonlinear interaction terms in Step 4 induces an overhead of $\sum_{l=1}^{nb_{\text{level}}} (N_{m-l}+1)^2(N_{m-l}+2)$ real numbers compared to the global memory of the DNS code.

5 Numerical results

5.1 Description of the simulations

In this Section, we present and compare forced DNS and DML simulations at four different Taylor microscale Reynolds numbers, in the range $Re_\lambda \in [60, 150]$. The computational parameters and the initial conditions were described in Section 2.4. In Table 2, we have reported several characteristic quantities corresponding to direct simulations.

All these quantities are space and time averages. The time averaging was performed over the whole interval $[0, T]$ during which the simulations were conducted. The mean values corresponding to the 64^3, 96^3 and 128^3 simulations are statistically steady. On the time interval $[T - 10\tau_e, T]$, the temporal variation of the kinetic energy K is less than 1.5% and of the order of 2.5% for the energy dissipation rate ε. The variations of the Reynolds number as well as the characteristic length and time scales listed in Table 2 are less than 1%. The 256^3 simulations was conducted only over 3.5 eddy-turnover times. Longer time integration at this resolution is prohibitive due to the CPU time requirement; one eddy-turnover time represents approximately 30 hours on one processor of the C90. As initial condition, we used the 128^3 DNS velocity field at time $19\tau_e$ so that the convergence

Table 2:
Characteristic values of the direct simulations.

Mesh	Δt	K	ε	Re_λ	τ_e	T/τ_e	L	λ	η	k_N/k_d
64^3	5×10^{-3}	0.24	0.022	61	4.1	24	1.64	0.76	4.92×10^{-2}	1.6
96^3	2.5×10^{-3}	0.27	0.023	84	3.8	25	1.59	0.60	3.32×10^{-2}	1.6
128^3	2.5×10^{-3}	0.24	0.020	117	3.6	26	1.514	0.44	2.04×10^{-2}	1.32
256^3	1.5×10^{-3}	0.26	0.022	150	3.5	3.5	1.46	0.32	1.34×10^{-2}	1.73

toward a statistically steady state was faster. The time variations of K over the last eddy-turnover time is of the order of 5% and a larger deviation ($\simeq$ 10%) is noted for ε.

For the 64^3, 96^3 and 128^3 simulations, the Reynolds numbers Re_λ are in agreement with the maximum allowable Reynolds numbers estimated by Kerr [4]. Such Reynolds numbers insure a fine enough accuracy to resolve the small scales of motions. In [8], the authors noted that $k_N/k_d \sim 1$ was a minimum resolution requirement and $k_N/k_d \sim 2$ was desirable in order to accurately compute the moments of the velocity gradients up to the sixth order. The ratio k_N/k_d is of the order of 1.3 for the 128^3 simulation and 1.7 for the other ones, so that the above criteria are satisfied.

As in [6], we have computed the following isotropy coefficient

$$\left(\sum_{\mathbf{k}\in S_N} |\hat{u}_{p,1}(\mathbf{k})|^2 / \sum_{\mathbf{k}\in S_N} |\hat{u}_{p,2}(\mathbf{k})|^2\right)^{1/2},$$

where $\hat{u}_{p,j}(\mathbf{k})$, $j=1,2$, are the components of $\hat{\mathbf{u}}(\mathbf{k})$ in the space orthogonal to the wave vector $\mathbf{k}$. This coefficient is close to 1.0 ± 0.1 in all the DNS and DML simulations considered here. Our simulated flows are then statistically isotropic.

In order to validate the DML procedure described in Section 4, we have performed simulations with the DML method with the same computational parameters and initial conditions used for the DNS. The parameters Tol_1, Tol_2 and ζ of the DML algorithm are reported in Table 3. We have denoted by $\langle - \rangle_j$ the average with respect to the number of cycles performed. The 96^3 and 128^3 DML simulations have been conducted until a statistically steady state was reached, i.e. $\sim$ 15 eddy-turnover times which corresponds to the time interval $[T, T-10\tau_e]$. The 64^3 and the 256^3 DML simulations were performed over the same time interval as the DNS ones, i.e. $[0,T]$. The DML simulations have been performed with different values of the parameter ζ which control the size of the local errors. Note that the cut-off levels decrease when ζ is increased, which is in agreement with the error analysis derived in Section 4. For the 64^3 simulation, the cut-off levels computed by the DML procedure are smaller than the Kolmogorov scale k_d, while for the other simulations they

Table 3:
Computational parameters and cut-off levels of the DML simulations.

Mesh	Tol_1	Tol_2	ζ	$\frac{\langle k_{N_{i(j)}} \rangle_j}{k_d}$	$\frac{\langle k_{N_{s(j)}} \rangle_j}{k_d}$	$\langle n_V(j) \rangle_j$	$\langle p(j) \rangle_j$	T/τ_e
64^3	2	2	3×10^{-2}	0.31	0.86	10	3	24
96^3	2	2	7×10^{-3}	0.51	1.3	10	5	15
128^3	2	2	5×10^{-3}	0.44	1.2	9	4	16
256^3	2	2	7.5×10^{-3}	0.76	1.5	9	5	3.5

lie in the range $[0.5k_d, 1.4k_d]$.
The following Sections are devoted to the comparison of the statistical properties of the DNS and DML simulations.

5.2 Long time stability of the DML procedure

On Figure 9, we have reported the relative differences between the kinetic energy K, as well as the energy dissipation rate ε, corresponding to the DNS and DML simulations. These differences increase when the lower cut-off level $k_{N_{i(j)}}$ is decreased, i.e. when the parameter ζ is increased. The more accurate results are obtained for the 256^3 resolution : a difference of the order of 1.15% is noted on K and less than 4% on ε. For the 96^3 and 128^3 simulations, the difference is less than 2.5% for the kinetic energy and of the order of 7% for the energy dissipation rate. The differences are larger for the 64^3 simulation i.e. 7.5% for the kinetic energy while the energy dissipation rate is over-estimated i.e. 30% larger than the DNS one. As it was noted before, the parameter ζ was chosen larger in this case so that the cut-off levels are smaller, i.e. $k_{N_{i(j)}} \sim 0.3k_d$. However, no growth of the errors was noted and a statistical steady state was reached.

Hence, the statistical steady states reached with the DML algorithm are close to the DNS ones. This indicates that the DML method is stable even on long time integration. There is no amplification of the local errors injected at each time iteration. As the effect of the dissipation is more important in the small scales equation, the errors may be slightly dissipated.

However, we can note that the differences on the computation of the kinetic energy are larger than ζ^2 which is a bound of the relative error tolerated at each time iteration (see Section 4). By comparing the time evolution of the kinetic energy corresponding to the 96^3 DNS and DML simulations (see Figure 10), it appears that the absolute distance between these quantities remains less than ζ^2 over approximately 5 eddy-turnover times. After this time period, the two curves oscillate near a similar average value but with different oscillating behaviors. This illustrates a well-known property of the dynamic of nonlinear systems. Indeed, even with very close initial data two solutions will separate after a transient period. The same behaviors can be observed on the energy dissipation rate ε and the energy injection rate $\langle \mathbf{g}_N \cdot \mathbf{u}_N \rangle$ (see Figure 10).

As it was mentioned in Section 2.4, the choice of the initial condition according to (2.26) avoids strong variations on the time evolution of the kinetic energy (see Figure 10). However, the forcing term induces an oscillating behavior of the time evolution of K with a large time period.

5.3 Spectra analysis

In the case of homogeneous turbulence, when the flow is assumed to be isotropic, the two-point correlation tensor and its spectral representation can be expressed in terms of the energy spectrum function $E(k)$ (see [16] and [17]). Therefore, this spectrum function is often used to characterize such turbulent flows. The energy spectrum depends on the energy transfer terms and on the energy dissipation spectrum; it then depends on how the energy is transferred and dissipated through the different scales of motion. Note that this information can not be accessed via the energy equation (2.25). In order to estimate the effect, on the representation of turbulence, of the DML numerical modeling of the small scales and of the nonlinear interaction term in the large scale equation, we compare hereafter the shape of the different energy spectra of the DNS and DML simulations.

In order to compare simulations with different Reynolds numbers, the energy spectrum functions are normalized i.e. $(\eta k)^{5/3}(\varepsilon\nu^5)^{-1/4}\ E(k)$ is plotted versus ηk on Figure 11. Moreover, $E(k)$ is a time average ; the time averaging has been performed over the time interval $[0, T]$ where T is the final time of the DML simulations listed in Table 3. By analyzing these spectra, we can determine whether there is significant truncation errors. Indeed, when the number of modes N retained in each spatial direction is not large enough an accumulation of energy appears at high-wavenumbers. Nevertheless, if the dissipation range is sufficiently extended, this spurious tail is not significant. By inspecting the high-wavenumbers of the DNS spectra, we note that the size of the upturns is acceptable. For the 64^3, 96^3 and 256^3 simulations they are of the same order as the ones appearing in [6] and [8]. The 128^3 simulation has the larger upturn ; as it was previously mentioned $k_N/k_d = 1.3$ in this case while $k_N/k_d \sim 1.7$ in the other ones. However, no amplifications were noted during the long time integration of the 128^3 DNS simulation. The high order moments may be slightly affected by this low resolution.

By comparing the DNS and DML spectra (Figure 11) at high-wavenumbers, we note that the upturns of the DNS spectra have been dissipated by the DML method. This numerical effect reflects a dissipative property of the modeling of the small scales via the equation (4.20). Moreover, this dissipative effect acts only on the smallest scales of the flow. Indeed, the shape of the energy spectrum is preserved for wavenumbers k smaller than the lower cut-off level $k_{N_{i(j)}}$. The analysis of the statistical properties of the simulated flows, presented in the following Section, confirms this point. We also note that the DML scheme reproduces the short $-5/3$ regime which extend from $k = 1$ through $k = 15$ for the 256^3 simulation. Hence, the DML method provides an accurate modeling of the nonlinear interaction term in the large scales equation especially at low wavenumbers.

Table 4:
Estimated values of the Kolmogorov constant C_K.

Re_λ	61	84	117	150
DNS	1.95	1.93	1.73	1.64
DML	1.83	1.80	1.75	1.61

On Figure 12, we have represented the DNS and DML energy and enstrophy spectra for the 128^3 and 256^3 resolutions. The DML and DNS spectra can not be distinguished for wavenumbers $k \le k_{N_{i(j)}}$ i.e. $k \le 0.44\ k_d$ for the 128^3 simulation and $k \le 0.76\ k_d$ for the 256^3 one. At larger wavenumbers it appears that the energy is slightly over-estimated. However, the shape of the energy spectrum is preserved and no energy accumulation is noted. This behavior is a consequence of the QS approximation applied to the scales lying in the range $[k_{N_{i(j)}}, k_{N_{s(j)}}]$. This small increase of the energy spectrum for $k \ge k_{N_{i(j)}}$ induces a larger increase of the enstrophy spectrum and therefore of the energy dissipation rate ε when the cut-off level $k_{N_{i(j)}}$ is decreased. This agrees with the relative errors on the computation of ε reported for the DML simulations in Section 5.2.

In [27] and [28], the authors suggested the following analytical form for the energy spectrum function of an isotropic homogeneous turbulent flow

$$E(k) \ = \ C_K \varepsilon^{\frac{2}{3}} k^{-\frac{5}{3}} e^{-\alpha_1 k\eta}, \text{ for } k \in [1, k_N], \tag{5.1}$$

where C_K is the Kolmogorov constant and $\alpha_1 = \left[2 C_K \Gamma\left(\frac{4}{3}\right)\right]^{\frac{3}{4}}$. The values of C_K corresponding to our simulations and obtained by fitting the energy spectra with the form (5.1), lie in the range $[1.64, 1.95]$ (see Table 4). In [6] and [8], the authors reported a value $C_K \sim 2$. In our case, C_K decreases slowly with respect to Re_λ so that for the 256^3 simulation the estimated value is close to the usual experimental one (~ 1.5) mentioned in [17]. A relative difference less than 2% appears between the DNS and DML values at the 128^3 and 256^3 resolutions. At lower resolutions, the differences are of the order of 7%.

5.4 The statistical properties of the simulated turbulent flows

In this Section, we present the high order statistical moments and the probability density functions of the velocity component u_1 and its derivatives. As in the previous Sections, we systematically compare the results of the DNS and DML simulations.

Let $u_i(\mathbf{x}, t)$ a velocity component, the m^{th} order moment of u_i is defined as

$$\mu_m \ = \ \langle u_i^m \rangle.$$

Table 5:
High order moments of the velocity component u_1 and its longitudinal and transverse gradients.

		u_1		$\partial u_1/\partial x_1$				$\partial u_1/\partial x_2$	
Mesh		F_4	F_6	$-F_3$	F_4	$-F_5$	F_6	F_4	F_6
64^3	DNS	2.57	10.00	0.44	4.38	6.47	46.0	5.91	98.9
	DML	2.53	9.66	0.33	3.99	4.93	43.2	4.58	59.5
96^3	DNS	2.54	9.63	0.45	4.78	7.55	61.4	6.54	135.5
	DML	2.55	9.73	0.45	4.69	7.60	60.1	5.97	105.2
128^3	DNS	2.70	11.31	0.47	5.09	8.33	72.05	7.39	193.5
	DML	2.70	11.65	0.43	5.06	7.90	75.50	6.42	131.8
256^3	DNS	2.78	12.12	0.55	5.78	11.73	106.2	8.79	307.1
	DML	2.79	12.17	0.54	5.83	12.01	116.2	8.56	346.2

The first order moment μ_1 is the mean value of u_i. Since an isotropic homogeneous field has zero mean value, the second moment (or variance) represents the mean-square departure from the mean value. The odd moments provides information on the symmetry of the distribution of u_i. Indeed, if the probability density function of u_i is symmetric with respect to the mean value, then all odd moments μ_{2m+1} are equal to zero. Non-dimensional moments are usually defined as

$$F_m(u_i(\mathbf{x},t)) \;=\; \frac{\mu_m}{\mu_2^{m/2}}.$$

The third non-dimensionalized moment $F_3(u_i)$ is called the *skewness* factor while the fourth one $F_4(u_i)$ is called the *kurtosis* or *flatness* factor. Functions with large kurtosis are characterized by the fact that they frequently take both very large and very small values. We recall that the even moments of a Gaussian distribution X are given by

$$F_{2m}(X) \;=\; \frac{(2m)!}{2^m m!},$$

so that $F_4(X) = 3.0$ and $F_6(X) = 15.0$.

In Table 5, we have reported the values of the high order moments of the velocity component u_1 and its longitudinal and transverse gradients $\frac{\partial u_1}{\partial x_1}$ and $\frac{\partial u_1}{\partial x_2}$ corresponding to the DNS and DML simulations. As in the previous Sections, these values are time averages. From experimental measurements, the distribution of the velocity components u_i are known to be approximately Gaussian (see [16] and [17]). This property was also observed on numerical simulations in [6]. For our simulations, the fourth order moment of u_1 lies in the range $F_4(u_1) \in [2.5, 2.8]$ and the sixth one $F_6(u_1) \in [9.5, 12.5]$; they are therefore close to the moments of a Gaussian distribution. These results are in agreement with those presented in [8]. Note that we observe a small increase of $F_4(u_1)$ and $F_6(u_1)$ with increasing Reynolds number. For the 96^3 and 256^3 simulations, the DML and DNS values of the moments of u_1 are similar with a difference less than 1%. A largest deviation is noted for the 64^3 and 128^3 simulations i.e. $\leq 1.6\%$ for $F_4(u_1)$ and $\sim 3.4\%$ for $F_6(u_1)$.

Experimental measures as well as numerical simulations (see [4], [6]) have predicted a longitudinal velocity derivative skewness factor in the range $-F_3\left(\frac{\partial u_1}{\partial x_1}\right) \in [0.4, 0.5]$. Indeed, Kerr [4] found that for $Re_\lambda \leq 20$ the skewness increases from 0 to 0.4 and then stabilizes around 0.45 for larger Re_λ. Moreover, the skewness factor was found to be independent of the Reynolds number and therefore essentially associated with the large scales (see [4], [5]). However, in [8] a weaker but consistent increase of $-F_3\left(\frac{\partial u_1}{\partial x_1}\right)$ with Re_λ was noted. We observe the same dependency on Re_λ, i.e. the skewness factor of our DNS simulations increases from 0.44 to 0.55. The dependency on the Reynolds number is more apparent on the fifth order moment lying in the range $-F_5\left(\frac{\partial u_1}{\partial x_1}\right) \in [6.5, 12]$ as in [8]. Hence, the assimmetry of the longitudinal velocity derivative distribution increases with Re_λ. For the 96^3 and 256^3 DML simulations, the values for these moments are very close to the DNS ones, i.e. the differences are less than 2.5%. In the two other cases, the distributions of the longitudinal velocity derivatives obtained with the DML algorithm appear to be slightly more symmetric than the DNS ones. Indeed, the odd moments of $\frac{\partial u_1}{\partial x_1}$ computed by DML are 25% (resp. 8.5%) smaller in the 64^3 (resp. 128^3) case.

The longitudinal velocity derivative flatness $F_4\left(\frac{\partial u_1}{\partial x_1}\right)$ is known to increase with the Reynolds number Re_λ (see [4], [5] and [8]). The fourth and sixth order moments of $\frac{\partial u_1}{\partial x_1}$ reflects the intermittency of the flow ; they are therefore associated with the small scale structures. In [4], the flatness obtained by DNS at $Re_\lambda \in [12, 80]$ behave as Re_λ^α with $\alpha \sim 0.18$. In our case, we find a larger value of α i.e. $\alpha \sim 0.28$; the values reported in [8] give a similar value i.e. $\alpha \sim 0.25$. The difference with the results presented by Kerr in [4] is probably due to the different range of the considered Reynolds numbers $Re_\lambda \in [60, 150]$ here and $[60, 170]$ in [8]. As for the odd moments, the 96^3 and 256^3 DML simulations reproduce accurately the property of the distribution of $\frac{\partial u_1}{\partial x_1}$. For the two other resolutions, the DML algorithm has a tendency to slightly reduce the even moments. Note that in the 256^3 case, the sixth order moment corresponding to the DML simulation is 10% larger than the DNS ones. However, for this simulation, the integration was conducted over 3.5 eddy-turnover times which is not enough for the higher order moments to reach a statistically steady state. This difference may reduce for longer time integration. On Figure 13, we have represented the time evolution of the longitudinal velocity derivative flatness $F_4\left(\frac{\partial u_1}{\partial x_1}\right)$ and $F_6\left(\frac{\partial u_1}{\partial x_1}\right)$ corresponding to the 128^3 simulation. Note that they are strongly oscillating functions of time. However, the time integration is long enough in this case so that the time averages of these curves converge to steady values. As it was noted previously, the DML and DNS curves behaves similarly over few time units (~ 3). After this transient period, they decorrelate but have close mean values.

The probability density functions of the longitudinal and transverse derivatives $\frac{\partial u_1}{\partial x_1}$ and $\frac{\partial u_1}{\partial x_2}$ corresponding to the 256^3 DNS and DML simulations are very similar even on the wings (see Figure 14). As it was noted in [6] and [8], the distribution of $\frac{\partial u_1}{\partial x_2}$ is more symmetric than the distribution of $\frac{\partial u_1}{\partial x_1}$.. This results in lower odd moments ; indeed, $-F_3(\frac{\partial u_1}{\partial x_2}) \in [0.06, 0.2]$ and is decreasing with Re_λ and $-F_5(\frac{\partial u_1}{\partial x_2}) \leq -0.5\ F_5(\frac{\partial u_1}{\partial x_1})$. Note that for an ideally isotropic flow, the third order moment $F_3(\frac{\partial u_1}{\partial x_2})$ must vanish (see [17]). Moreover, the distribution of $\frac{\partial u_1}{\partial x_2}$ takes larger extremal values inducing larger even moments as it can be noted in Table 5. As a consequence of the larger width of the distribution of $\frac{\partial u_1}{\partial x_2}$, the differences between the DML and DNS values are increased compared to those of the

Table 6:
Memory size (MegaWords) and CPU time (hours) of the DNS and DML codes.

Mesh	Memory size (DNS)	Overhead (DML/DNS)	CPU time (DNS)	CPU time (DNS/DML)
64^3	2.62	18%	47.4	3.05
96^3	8.85	31%	207	2.7
128^3	21	21%	650	2.95
256^3	168	32%	102	2.71

even moments of $\frac{\partial u_1}{\partial x_1}$. Again, the more accurate DML simulations correspond to the 96^3 and 256^3 simulations.

5.5 The computational efficiency of the DML method

As it has been noted in Section 4.4, Step 4 of the DML algorithm required the storage of the nonlinear interaction term on every coarse level. This induces an overhead of the memory which can be estimated as $\sum_{l=1}^{nb_{\text{level}}}(N_{m-l}+1)^2(N_{m-l}+2)$. The memory of the DNS code is of the order of $10 \times N^3$ real numbers. In Table 6, we have reported the memory required by the DNS code for the considered simulations and the overhead DML/DNS. Note that this overhead is independent of the resolution ; it depends of the sequence of coarse levels retained.

The 64^3, 96^3 and 128^3 simulations have been performed on a Cray YMP-EL (4 processors) while the 256^3 requiring much more memory has been computed on a Cray C90 (8 processors). The DNS and DML codes exhibit similar computational performances (vectorization and multi-tasking). However, the DML method computing on coarse levels require less operations than the DNS (see (4.27)). This induces a noticeable reduction of the CPU time. Indeed, the DML code runs approximately 3 times faster than the DNS one (see Table 6).

6 Conclusion

In this paper, we have performed simulations of three dimensional homogeneous turbulent flows at Reynolds numbers in the range $Re_\lambda \in [60, 150]$. In each case, we have analyzed and compared the results obtained with the DML algorithm described in Section 4 and with direct simulations. The DML method consists in computing the small scales with less accuracy than the large ones. The spectrum is splitted into three parts : the first one, $k \leq k_{N_{i(j)}}$, corresponds to the resolved (large) scales, the second one $k \in [k_{N_{i(j)}}, k_{N_{s(j)}}]$ is a transition range (intermediate scales) allowing an adaptative numerical treatment with respect to the time and the cut-off wavenumbers. Moreover, this part of the spectrum provides local interaction for the resolved scales near the cut-off length scale. In the third part i.e. $k \in [k_{N_{s(j)}}, k_N]$, the small scales are computed every $2(s(j) - i(j))$ iterations and are assumed to be slaved by the large ones.

In Section 5, we have shown that this adaptative numerical procedure provides an accurate description of turbulent flows. By comparing the statistical steady states reached by the DML simulations and the DNS, we have shown the long time stability of the procedure. No growth of the local errors injected at each time iteration was noted. All the spatial averages as the kinetic energy, the enstrophy and the characteristic length scales have very close values. Moreover, the energy spectra have similar decays for the resolved scales and no energy pile-up appears at high wavenumbers. Finally, the statistical properties of the velocity and its derivatives are accurately reproduced, namely the high order statistics are of the same order of magnitude for both methods. The dependency of the accuracy of the DML procedure upon the parameter ζ used to control the size of the local errors was also studied.

In the 96^3, 128^3 and 256^3 DML simulations, the cut-off wavenumbers lies in the range $k \in [0.5\ k_d, 1.25\ k_d]$. Compared with direct simulations, the CPU time is reduced by a factor of the order of 3. In the 64^3 DML simulation, the cut-off levels are below the Kolmogorov wavenumber i.e. they lie in the range $k \in [0.3\ k_d, 0.8\ k_d]$. In such a case, a larger deviation between the DNS and DML simulations is noted over long time integration. However, a statistically steady state having similar properties is still reached. The QS approximation applied to the intermediate scales induces a small increase of the energy spectrum in the corresponding range of wavenumbers. This results in lower high order statistics. Hence, a numerical treatment more accurate than the QS approximation has to be applied to these scales in order to decrease the cut-off levels below the value $k_d/4$ which corresponds to the peak of the spectrum function associated with velocity time derivative.

Hence, the numerical results presented here confirm the fact that the small scales of motion as well as the nonlinear interaction term (subgrid scale tensor) can be computed less accurately than the large ones. This results in a noticeable reduction of the number of operations and therefore in CPU time. Note that other possibilities can be considered. For instance, the small scales can be computed with less accurate schemes, requiring less computational efforts. Several theoretical works have shown that larger time steps can be used for the computation of the small scales; see for instance, [29], [30] and [31]. Related numerical studies are actually in progress and will be presented elsewhere.

Acknowledgments

As computational resources we used the Cray YMP-EL (4 processors) of the LMA, University Blaise Pascal (France) and the Cray C90 (8 processors) of the Supercomputing Center IDRIS of CNRS (France).
The authors would like to specially thank E. Gondet (IDRIS, CNRS, France) for his help in improving the vectorized and multi tasked performances of the codes on the Cray C90.

References

[1] S.A. Orszag and G.S. Patterson (1972), *Numerical simulation of three-dimensional homogeneous isotropic turbulence*, Phys. Rev. Lett., **28**, 76.

[2] E.D. Siggia and G.S. Patterson (1978), *Intermittency effects in a numerical simulation of stationary three-dimensional turbulence*, J. Fluid Mech., **86** (3), 567-592.

[3] E.D. Siggia (1981), *Numerical study of small-scale intermittency in three-dimensional turbulence*, J. Fluid Mech., **107**, 375-406.

[4] R.M. Kerr (1985), *Higher-order derivative correlations and the alignment of small-scale structures in isotropic numerical turbulence*, J. Fluid Mech., **153**, 31-58.

[5] Z.S. She, E. Jackson and S.A. Orszag (1988), *Scale-dependent intermittency and coherence in turbulence*, J. Sci. Comput., **3** (4), 407-434.

[6] A. Vincent and M. Meneguzzi (1991), *The spatial structure and statistical properties of homogeneous turbulence*, J. Fluid Mech., **225**, 1-20.

[7] S. Chen, G.D. Doolen, R.H. Kraichnan and Z.S. She (1993), *On statistical correlations between velocity increments and locally averaged dissipation in homogeneous turbulence*, Phys. Fluids A, **5**(2), 458-463.

[8] J. Jimenez, A.A. Wray, P.G. Saffman and R.S. Rogallo (1993), *The structure of intense vorticity in isotropic turbulence*, J. Fluid Mech., **255**, 65-90.

[9] P.R. Woodward, D.H. Porter, B.K. Edgar, S. Anderson and G. Bassett (1995), *Parallel computation of turbulent fluid flow*, Comp. Appl. Math., **14** (1), 97-105.

[10] C. Foias, O.P. Manley and R. Temam (1988), *Modeling on the interaction of small and large eddies in two dimensional turbulent flows*, Math. Mod. and Num. Anal. (M2AN), **22** (1), 93-114.

[11] F. Jauberteau (1990), *Résolution numérique des équations de Navier-Stokes instationnaires par méthodes spectrales. Méthodes de Galerkin non linéaire*, Thesis, Université de Paris-Sud.

[12] T. Dubois, F. Jauberteau and R. Temam (1993), *Solution of the incompressible Navier-Stokes equations by the nonlinear Galerkin method*, J. Sci. Comput., **8** (2), 167-184.

[13] A. Debussche, T. Dubois and R. Temam (1995), *The nonlinear Galerkin Method: a multiscale method applied to the simulation of homogeneous turbulent flows*, Theoret. Comput. Fluid Dynamics, **7** (4), 279-315.

[14] F. Jauberteau, C. Rosier and R. Temam (1989), *The nonlinear Galerkin method in computational fluid dynamics*, Applied Numerical Mathematics, **6**, 361-370.

[15] F. Jauberteau, C. Rosier and R. Temam (1990), *A nonlinear Galerkin method for the Navier-Stokes equations*, Computer Math. Appl. Mechanics and Engineering, **80**, 245-260.

[16] G.K. Batchelor (1953), *Theory of homogeneous turbulence*, Cambridge University Press.

[17] A.S. Monin and A.M. Yaglom (1975), *Statistical fluid mechanics*, **2**, MIT Press.

[18] O. Reynolds (1895), *On the dynamical theory of incompressible viscous fluids and the determination of the criterion*, Phil. Trans. Roy. Soc. London A, **186**, 123-164.

[19] J. Smagorinsky (1963), *General circulation experiments with the primitive equations: I-The basic experiment,* Monthly Weather Review, **91**, 99-164.

[20] C. Canuto, Y. Hussaini, A. Quarteroni and T.A. Zang (1988), *Spectral methods in fluid dynamics,* Springer Verlag, New York.

[21] J.W. Deardorff (1970), *A numerical study of three dimensional turbulent channel flow at large Reynolds numbers,* J. Fluid Mech., **41**, 453-480.

[22] U. Schumann (1975), *Subgrid scale model for finite difference simulations of turbulent flows in plane channels and annuli,* J. Comput. Phys., **18**, 376-404.

[23] P. Moin and J. Kim (1982), *Numerical investigation of turbulent channel flow,* J. Fluid Mech., **118**, 341-377.

[24] G. Erlebacher, M.Y. Hussaini, C.G. Speziale and T.A. Zang (1992), *Toward the large-eddy simulation of compressible turbulent flows,* J. Fluid Mech., **238**, 155-185.

[25] T. Dubois, F. Jauberteau and Y. Zhou (1997), *Influences of subgrid scale dynamics on resolvable scale statistics in large-eddy simulations,* Physica D, **100**, 390-406.

[26] S.A. Orszag (1973), *Lectures on the statistical theory of turbulence*, in Proceedings of the Summer School in Theoretical Physics, Les Houches.

[27] L.M. Smith and W.C. Reynolds (1991), *The dissipation-range spectrum and the velocity-derivative skewness in turbulent flows*, Phys. Fluids A, **3**, 992.

[28] O.P. Manley (1992), *The dissipation range spectrum*, Phys. Fluids A, **4** (6), 1320-1321.

[29] J.L. Lions, R. Temam and S. Wang (1996), *Splitting up methods and numerical analysis of some multiscale problems*, Computational Fluid Dynamics Journal, special issue dedicated to A. Jameson, **5** (2), 157-202.

[30] R. Temam (1996), *Multilevel methods for the simulation of turbulence. A simple model*, J. Comput. Phys., **127**, 309-315.

[31] J.B. Burie and M. Marion (1997), *Multi-level methods in space and time for the Navier-Stokes equations,* SIAM J. Num. Anal., **34**.

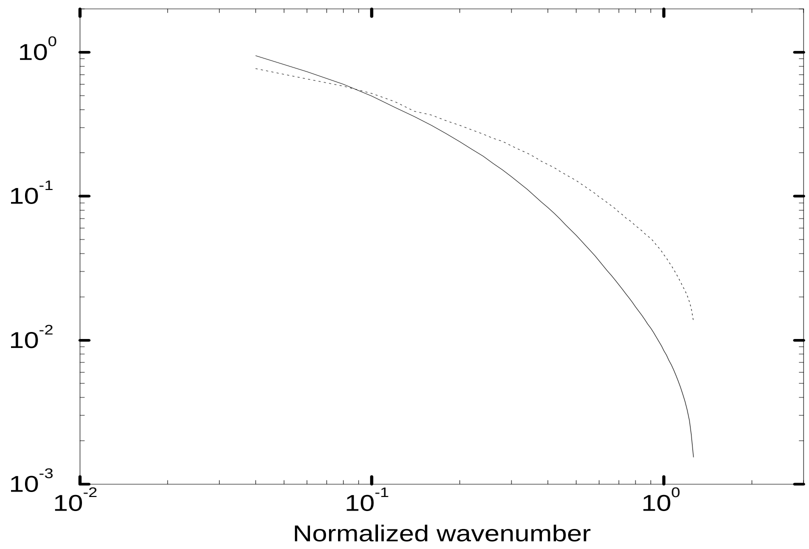

Figure 1: $|\mathbf{z}_{N_1}^N|_2/|\mathbf{y}_{N_1}|_2$ (solid line) and $|P_{N_1}B_{int}(\mathbf{y}_{N_1}, \mathbf{z}_{N_1}^N)|_2/|P_{N_1}B(\mathbf{y}_{N_1}, \mathbf{y}_{N_1})|_2$ (dotted line) as functions of the normalized wavenumber ηk_{N_1}.

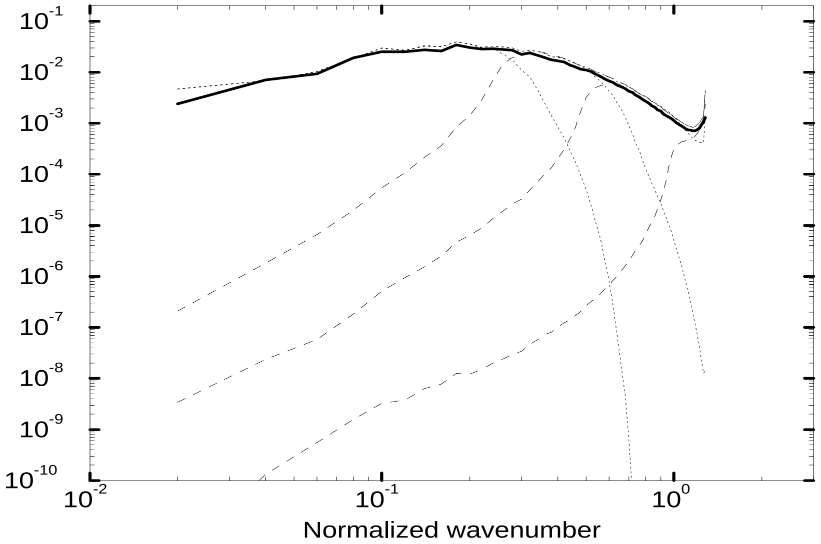

Figure 2: $NL(k, k_{N_1})$ (dotted line), $NL_{int}(k, k_{N_1})$ (dashed line), for $k_{N_1} = 12,\ 24,\ 48$, and $T(k)$ (solid line) as functions of the normalized wavenumber ηk.

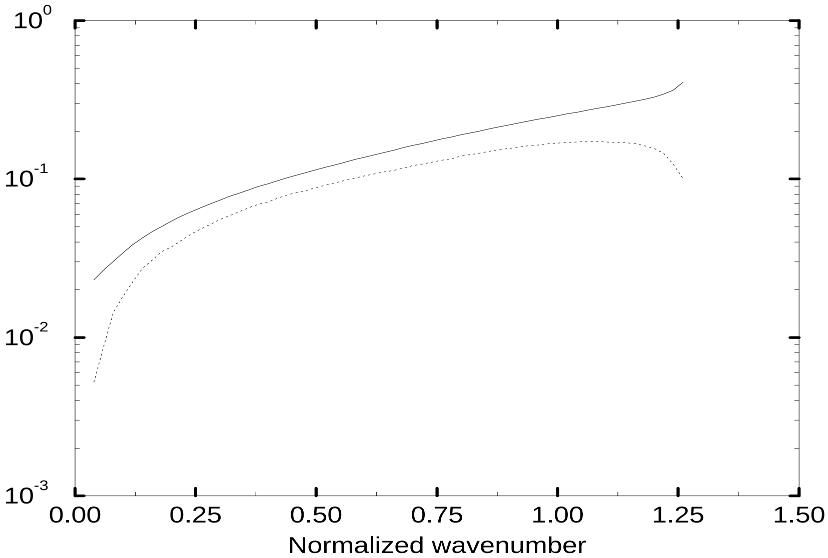

Figure 3: $(k_N u_\infty)^{-1}|\dot{\mathbf{z}}^N_{N_1}|_2/|\mathbf{z}^N_{N_1}|_2$ (solid line) and $(k_N u_\infty)^{-1}|P_{N_1}\dot{B}_{int}(\mathbf{y}_{N_1}, \mathbf{z}^N_{N_1})|_2/|P_{N_1}B_{int}(\mathbf{y}_{N_1}, \mathbf{z}^N_{N_1})|_2$ (dotted line) as functions of ηk_{N_1}.

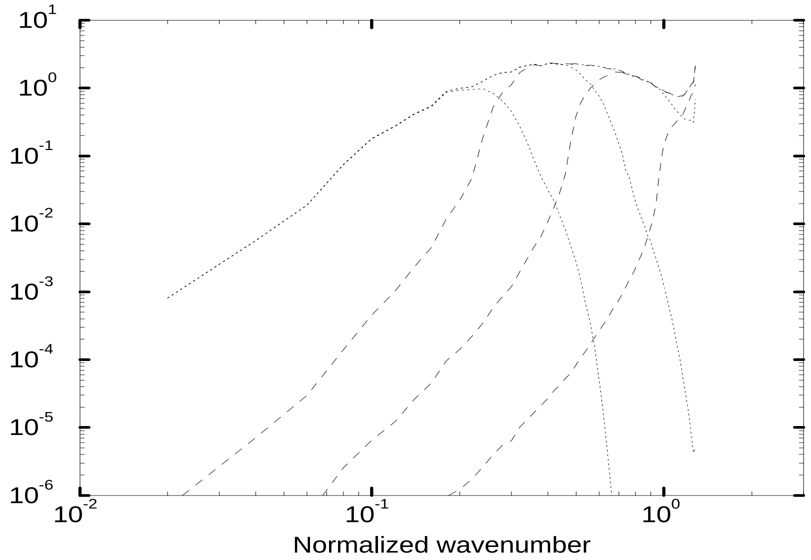

Figure 4: $TNL(k, k_{N_1})$ (dotted line), $TNL_{int}(k, k_{N_1})$ (dashed line), for $k_{N_1} = 12,\ 24,\ 48$, as functions of the normalized wavenumber ηk.

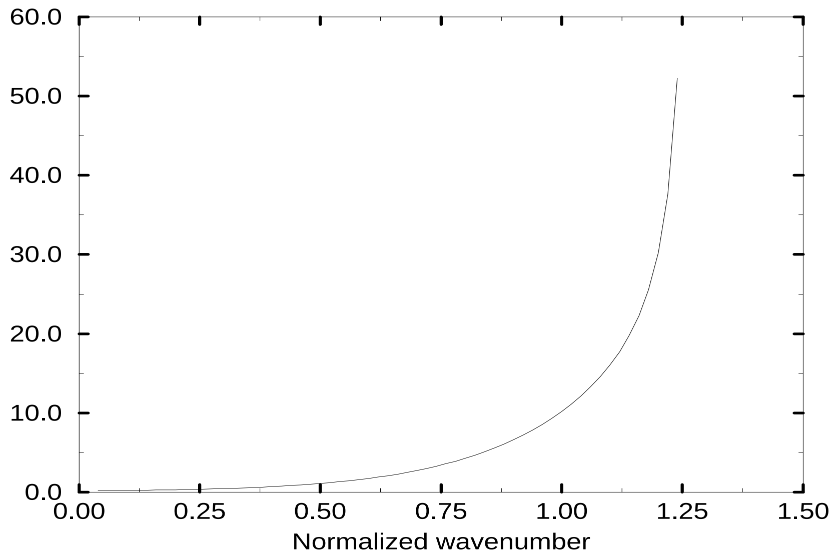

Figure 5: Ratio $|\dot{\mathbf{z}}^N_{k_d/2}|_2/|\dot{\mathbf{z}}^N_{N_1}|_2$ as a function of ηk_{N_1}.

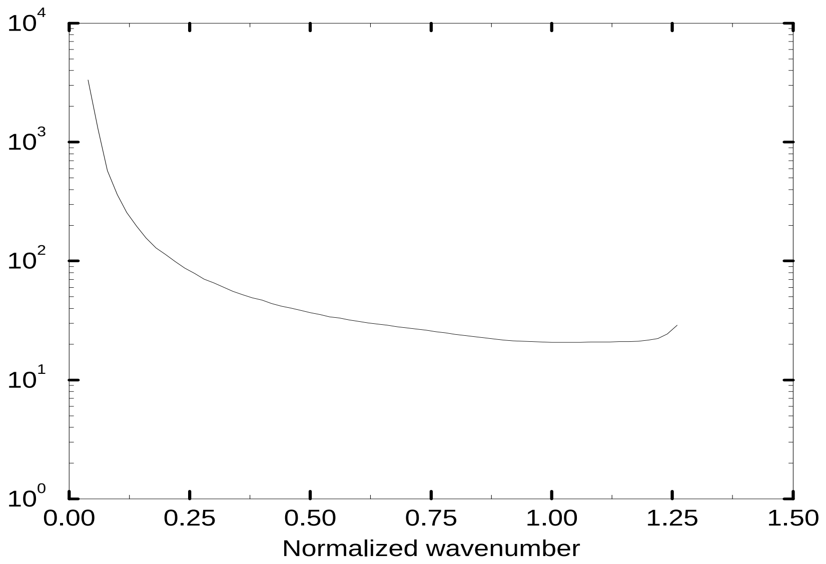

Figure 6: Ratio $(k_N u_\infty)|\dot{\mathbf{z}}_{N_1}^N|_2/|P_{N_1}\dot{B}_{int}(\mathbf{y}_{N_1}, \mathbf{z}_{N_1}^N)|_2$ as a function of ηk_{N_1}.

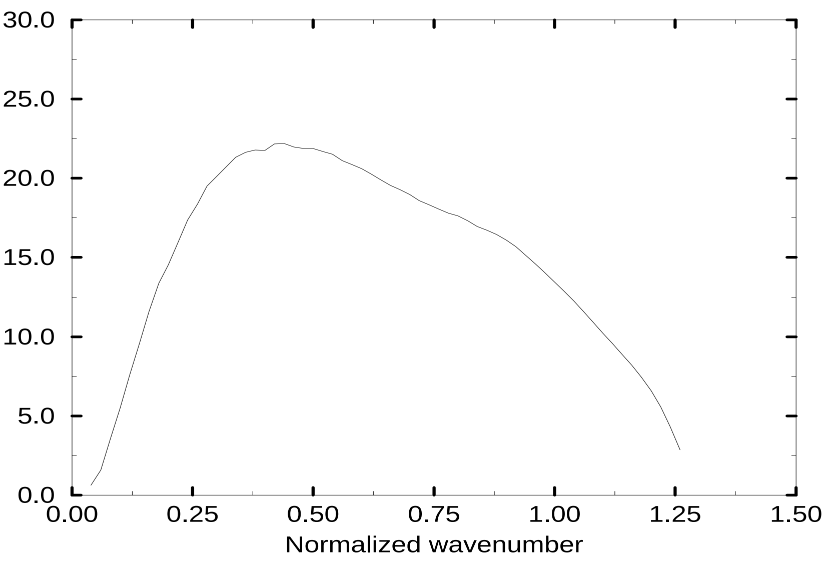

Figure 7: $|P_{N_1}\dot{B}_{int}(\mathbf{y}_{N_1}, \mathbf{z}_{N_1}^N)|_2$ as a function of ηk_{N_1}.

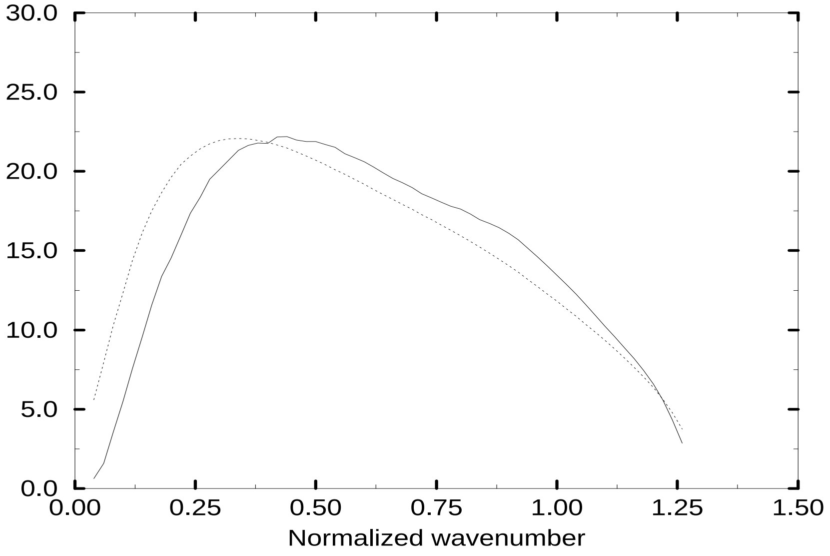

Figure 8: $|P_{N_i}\dot{B}_{int}(\mathbf{y}_{N_i}, \mathbf{z}^N_{N_i})|_2$ (solid line) and $\dfrac{|P_{N_i}B(\mathbf{y}_{N_i}, \mathbf{y}_{N_i})|_2|\dot{\mathbf{z}}^N_{N_i}|_2||\mathbf{z}^N_{N_i}||}{4\ |\mathbf{z}^N_{N_i}|_2||\mathbf{y}_{N_i}||}$ (dotted line) as functions of ηk_{N_1}.

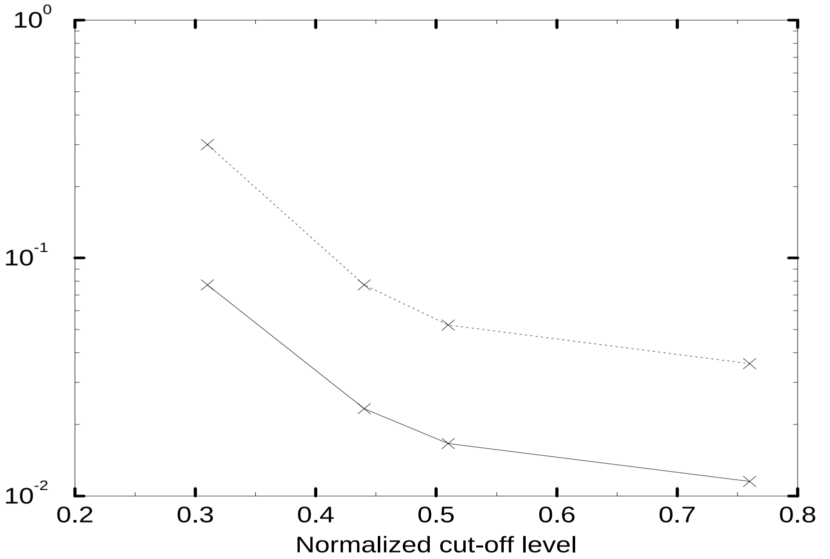

Figure 9: Relative differences between the DNS and DML kinetic energy (solid line) and energy dissipation rate (dotted line) plotted as a function of $\langle k_{N_{i(j)}}\rangle_j / k_d$.

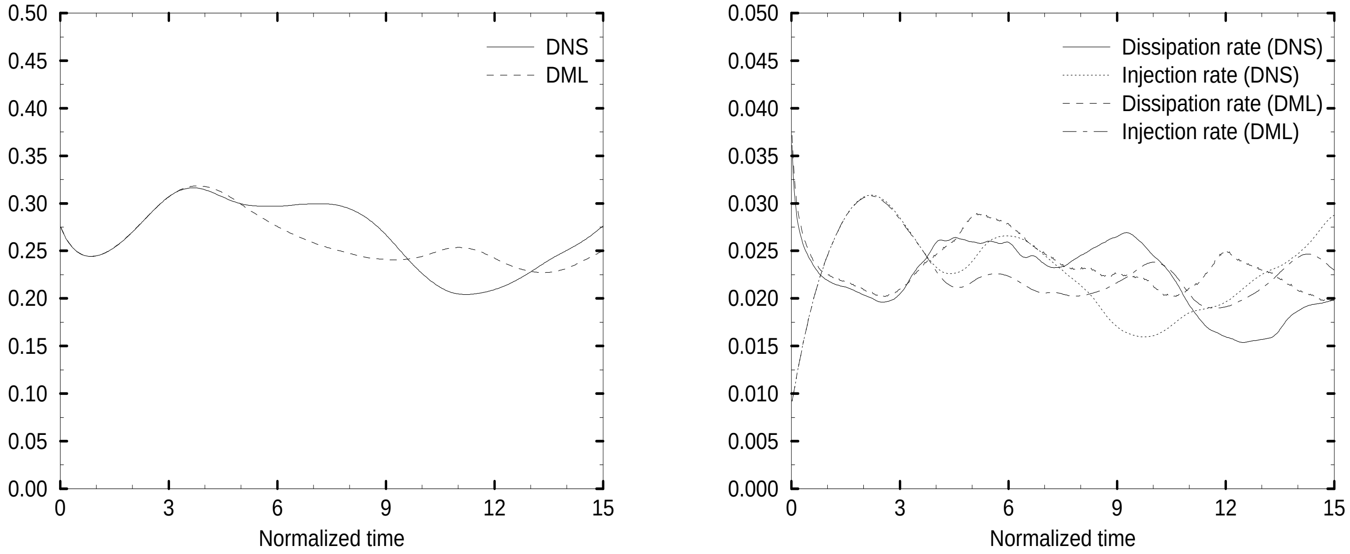

Figure 10: Time evolution of the kinetic energy K (left), of the energy dissipation rate ε and energy injection rate $\langle \mathbf{g}_N \cdot \mathbf{u}_N \rangle$ (right) as functions of the normalized time t/τ_e.

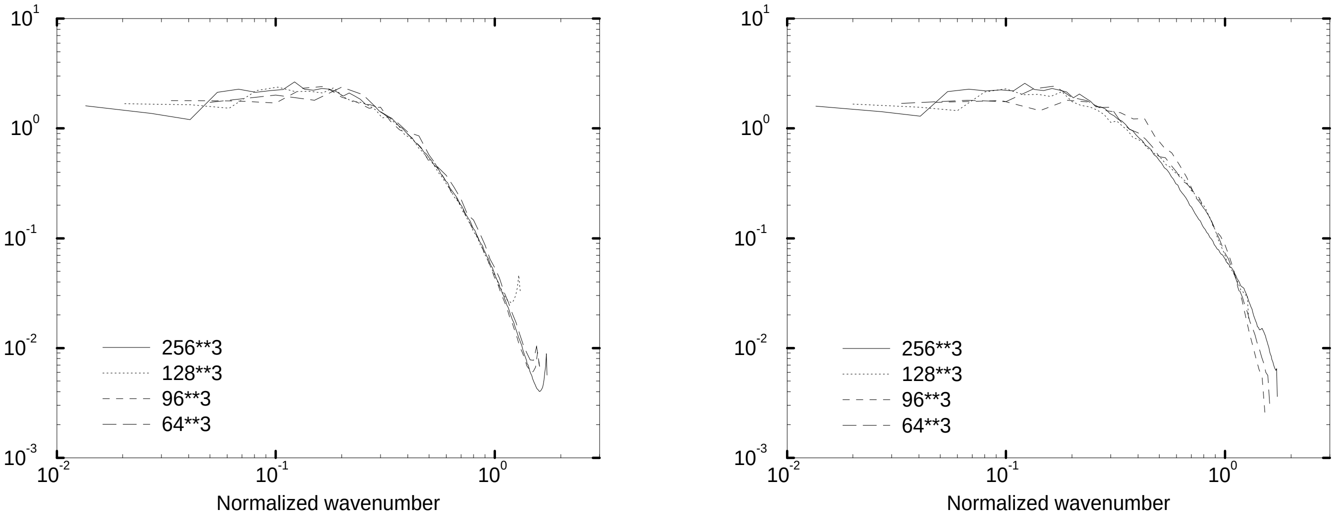

Figure 11: Normalized energy spectra $(\eta k)^{5/3}(\varepsilon\nu^5)^{-1/4}\ E(k)$ of the DNS (left) and DML (right) simulations plotted as functions of ηk.

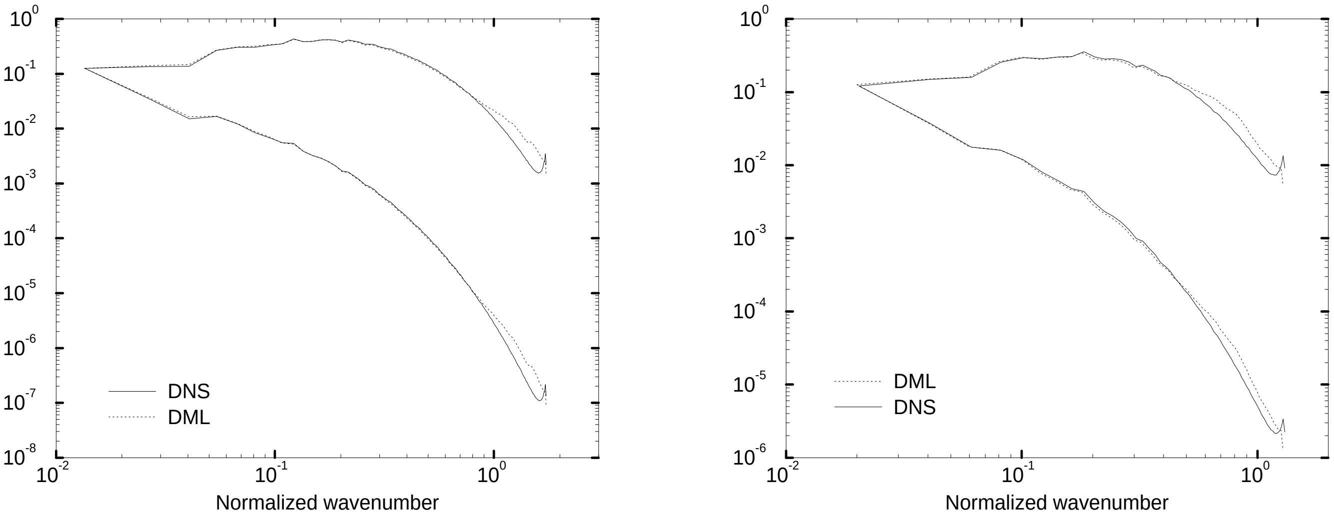

Figure 12: Energy $E(k)$ and enstrophy $\varepsilon(k)$ spectra of the 256^3 (left) and 128^3 (right) simulations plotted as functions of ηk.

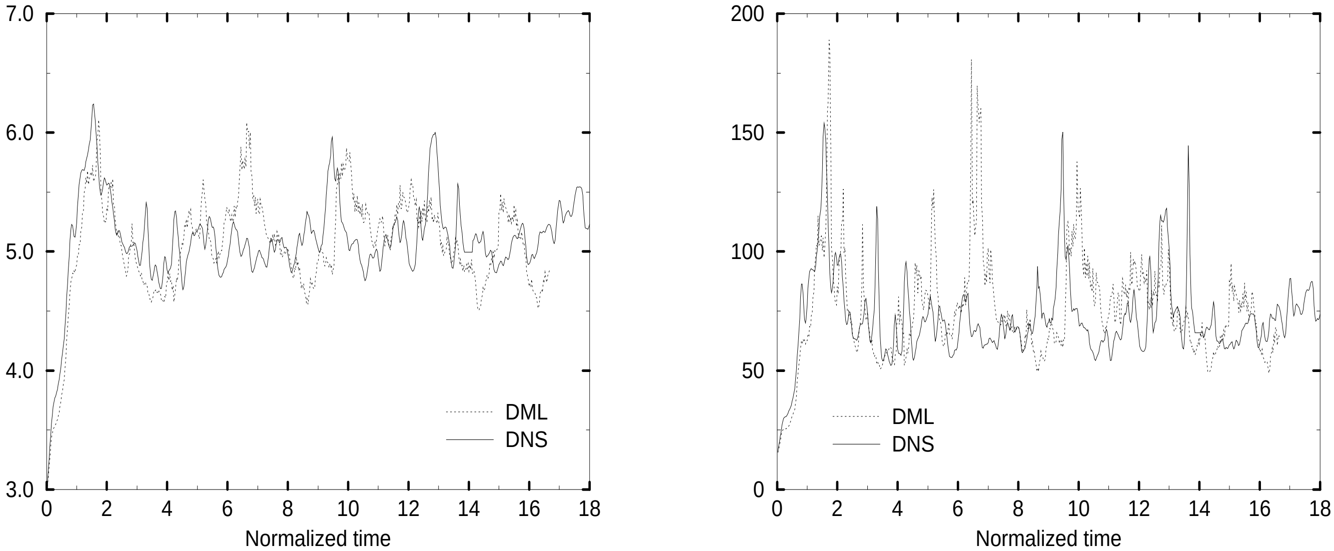

Figure 13: Time evolution of the fourth $F_4(\partial u_1/\partial x_1)$ (left) and sixth $F_6(\partial u_1/\partial x_1)$ (right) order moments of the longitudinal velocity derivative plotted as functions of t/τ_e.

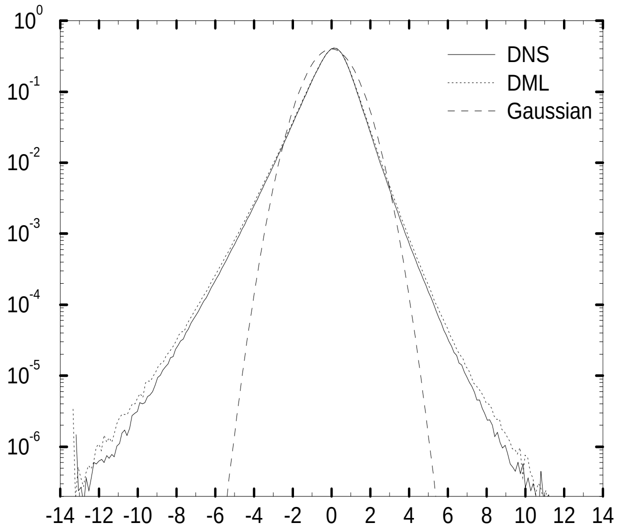

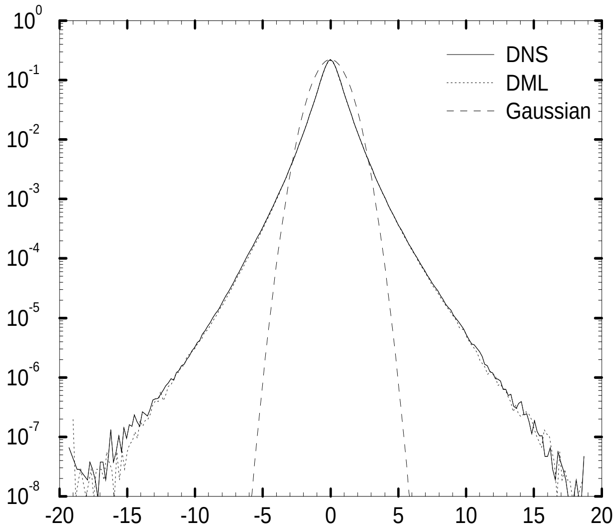

Figure 14: Probability density functions for $\partial u_1/\partial x_1$ (left) and $\partial u_1/\partial x_2$ (right) normalized so that $\sigma = 1$, shown together with a Gaussian distribution.